

Mapping the mesospheric CO₂ clouds on Mars: MEx/OMEGA and MEx/HRSC observations and challenges for atmospheric models

A. Määttänen^{a,*}, F. Montmessin^a, B. Gondet^b, F. Scholten^c, H. Hoffmann^c, F. González-Galindo^{d,1}, A. Spiga^e, F. Forget^d, E. Hauber^c, G. Neukum^f, J.-P. Bibring^b, J.-L. Bertaux^a

^aLaboratoire Atmosphères, Milieux, Observations Spatiales, CNRS/UVSQ/UPMC, 11 boulevard d'Alembert, 78280 Guyancourt, France

^bInstitut d'astrophysique spatiale, Bâtiment 121, Université Paris XI, 91405 Orsay cedex, France

^cGerman Aerospace Center (DLR), Institute of Planetary Research, Rutherfordstraße 2, 12489 Berlin, Germany

^dLaboratoire de météorologie dynamique, CNRS/UPMC, 4 place Jussieu, 75252 Paris cedex 05, France

^eDepartment of Physics and Astronomy, The Open University, Milton Keynes, United Kingdom

^fFreie Universität, Fachrichtung Planetologie und Fernerkundung, Malteserstr. 74-100, D-12249 Berlin, Germany

ARTICLE INFO

Article history:

Received 2 July 2009

Revised 20 May 2010

Accepted 24 May 2010

Available online 1 June 2010

Keywords:

Terrestrial planets

Mars, Atmosphere

Atmospheres, Structure

ABSTRACT

This study presents the latest results on the mesospheric CO₂ clouds in the martian atmosphere based on observations by OMEGA and HRSC onboard Mars Express. We have mapped the mesospheric CO₂ clouds during nearly three martian years of OMEGA data yielding a cloud dataset of ~60 occurrences. The global mapping shows that the equatorial clouds are mainly observed in a distinct longitudinal corridor, at seasons $L_s = 0-60^\circ$ and again at and after $L_s = 90^\circ$. A recent observation shows that the equatorial CO₂ cloud season may start as early as at $L_s = 330^\circ$. Three cases of mesospheric midlatitude autumn clouds have been observed. Two cloud shadow observations enabled the mapping of the cloud optical depth ($\tau = 0.01-0.6$ with median values of 0.13–0.2 at $\lambda = 1 \mu\text{m}$) and the effective radii (mainly 1–3 μm with median values of 2.0–2.3 μm) of the cloud crystals. The HRSC dataset of 28 high-altitude cloud observations shows that the observed clouds reside mainly in the altitude range ~60–85 km and their east–west speeds range from 15 to 107 m/s. Two clouds at southern midlatitudes were observed at an altitude range of 53–62 km. The speed of one of these southern midlatitude clouds was measured, and it exhibited west–east oriented speeds between 5 and 42 m/s. The seasonal and geographical distribution as well as the observed altitudes are mostly in line with previous work. The LMD Mars Global Climate Model shows that at the cloud altitude range (65–85 km) the temperatures exhibit significant daily variability (caused by the thermal tides) with the coldest temperatures towards the end of the afternoon. The GCM predicts the coldest temperatures of this altitude range and the season $L_s = 0-30^\circ$ in the longitudinal corridor where most of the cloud observations have been made. However, the model does not predict supersaturation, but the GCM-predicted winds are in fair agreement with the HRSC-measured cloud speeds. The clouds exhibit variable morphologies, but mainly cirrus-type, filamented clouds are observed (nearly all HRSC observations and most of OMEGA observations). In ~15% of OMEGA observations, clumpy, round cloud structures are observed, but very few clouds in the HRSC dataset show similar morphology. These observations of clumpy, cumuliform-type clouds raise questions on the possibility of mesospheric convection on Mars, and we discuss this hypothesis based on Convective Available Potential Energy calculations.

© 2010 Elsevier Inc. All rights reserved.

1. Introduction

The major constituent of the martian atmosphere, CO₂, condenses as surface ice on the winter poles and as clouds in the coldest parts of the atmosphere, such as the polar night (Pettengill and

Ford, 2000; Ivanov and Muhleman, 2001). A recent discovery has been the formation of CO₂ clouds not only at the winter pole, but also at high altitudes near the equator in spring and summer (Formisano et al., 2006; Montmessin et al., 2006a,b, 2007; Clancy et al., 2007). Very recently these clouds have been also observed at northern midlatitudes in late autumn (Inada et al., 2007, this paper; McConnochie et al., 2009) and in the corresponding southern season (Montmessin et al., 2007, and this paper). Such clouds have not been predicted by atmospheric models and are challenging our understanding of the martian atmosphere. Revealing the atmo-

* Corresponding author.

E-mail address: anni.maattanen@latmos.ipsl.fr (A. Määttänen).

¹ Present address: Instituto de Astrofísica de Andalucía, CSIC, P.O. Box 3004, 18080 Granada, Spain.

spheric processes leading to CO₂ cloud formation will require not only more modeling, but also additional observations.

Montmessin et al. (2007) published the first study of the spectral signature and properties of these clouds using OMEGA data. In this study we are investigating these clouds more thoroughly using again data from the OMEGA instrument, and additional, complementary HRSC observations. We have analysed the observations to map the spatial and seasonal distribution of the clouds and to study cloud internal structures. OMEGA nadir observations have been the starting point of the study providing information on the orbit of detection, location and timing of the cloud, as well as possible interannual variations between the several consecutive years of MEx observations. We have thoroughly analysed the OMEGA orbits to map the cloud signatures. We have extended the analysis to more detailed studies, such as determination of cloud properties using observations of cloud shadows. Although the cloud main spectral signature resides in the near-infrared, the clouds can be seen in the visible wavelengths as well. This enables visible imaging instruments, such as HRSC, to detect the clouds. The HRSC instrument is a stereo-imager that looks at the martian surface through several filters. The clouds are seen mainly through two filters, which enables direct calculation of the cloud altitude from the imaging data, as well as the east–west movement of the clouds, giving information on mesospheric wind speeds.

This paper extends the analysis of OMEGA data performed by Montmessin et al. (2007) with a larger dataset of about 60 cloud occurrences we have acquired within the three martian years of observations (Mars Years 27–29). We introduce as well the HRSC dataset with selected results. Another study using HRSC data is published elsewhere (Scholten et al., *in press*).

In addition, we compare the cloud observations to the predictions of the LMD Mars Global Climate Model (LMD-MGCM) of mesospheric temperatures and winds.

OMEGA observations of clumpy, round, cumuliform clouds already introduced and evaluated as convective-type clouds by Montmessin et al. (2007) are reanalysed here. We try to evaluate the possibility of mesospheric convection in the martian atmosphere with the help of Convective Available Potential Energy (CAPE) calculations.

2. Instruments and observation types used

2.1. OMEGA

OMEGA (Observatoire pour la mineralogie, l'eau, des glaces et l'activité) is a visible and near-infrared imaging spectrometer functioning in two channels in the wavelength range 0.38–5.1 μm (Bibring et al., 2004). The VNIR channel covers wavelengths from 0.38 to 1.05 μm and the SWIR channel wavelengths 0.93–5.1 μm . The SWIR channel operates in two ranges of 0.93–2.73 μm (SWIRC-channel) and 2.55–5.1 μm (SWIRL-channel). For this study we are using OMEGA nadir data only, and mainly the SWIRL-channel for the cloud detection. OMEGA can observe in nadir mode with satellite–Mars distance between 400 and 4000 km. The OMEGA orbits are divided in observational sessions, hereinafter called 'cubes' or 'sessions', which are namely three-dimensional data cubes containing the image and spectral data (dimensions x , λ , y). These OMEGA sessions are named with the convention #orbit_session (for example, #501_2), which is used hereinafter. The spectra consist of spectral elements or 'spectels', which are simply equivalent to the spectral wavelength bins. For details on the instrument and its general calibration we refer the reader to Bibring et al. (2004), except for the calibration of the SWIRL-channel during non-nominal stages, described in Jouget et al. (2008).

2.2. HRSC

The HRSC (High-Resolution Stereo Camera, Jaumann et al., 2007) is a stereo-imaging system that images the martian surface through different filters and in stereo. The observations concentrate in periods with the satellite–Mars distance less than 1000 km with emphasis on distances below 750 km. Some observations have been made from about 2500 km distance. The imaging of the surface naturally includes observations of atmospheric phenomena, such as dust storms, water ice clouds, and also CO₂ clouds as implied by their high altitudes and similar locations/seasons with spectrally identified CO₂ clouds.

In most cases, HRSC sees the clouds with two different color filters, blue (440 ± 45 nm) and green (530 ± 45 nm), one looking slightly forward from the nadir pointing, the other slightly backward. These different viewing geometries yield a stereo angle of 6.6° along the orbit between the two color images and an apparent change in location of the cloud in north–south direction between the two images, which enables an accurate (uncertainties generally less than ± 2 km) determination of cloud altitudes. The cloud altitudes refer to the altitude of the level where the cloud is optically thick enough to be seen by HRSC. However, a calculation of the exact altitude of this level has not been conducted. The distinct viewing angles also result in a difference in time (5–15 s) for the two channels in imaging the same feature. Time-related spatial displacements of the feature in across-track direction can easily be detected and allow to derive the east–west oriented wind speeds with accuracies of about ± 15 –20 m/s. This should be directly proportional to the winds advecting the clouds, thus giving a measure of mesospheric wind speeds. Naturally, if the cloud movement also has a component in the north–south direction, this cannot be distinguished from the apparent movement of the cloud caused by the satellite movement, and it will thus introduce a small error in the altitude determination. A detailed discussion of the HRSC cloud measurement technique, the analysis method, and the achievable accuracies can be found in Scholten et al. (*in press*).

HRSC images have been checked for the Mars Years 27 and 28 (two first years of observation) so far mainly in those orbits where OMEGA detects clouds (see Table 3). A thorough analysis of all available HRSC imagery with respect to mesospheric cloud observations and measurements was performed in the beginning of the third year of observations (MY 29, orbit numbers 5049–5390). This period covers joint cloud observations by HRSC and OMEGA as well as stand-alone detections by one of the instruments (see Table 4). Scholten et al. (*in press*) describe the HRSC observations in MY 29 more in detail.

3. Results from nadir observations of the OMEGA instrument

3.1. Statistical method for cloud detection and mapping

As described by Montmessin et al. (2007), the OMEGA spectra show a particular spectral signature related to CO₂ clouds (see Fig. 1) exhibiting one or two distinct peaks that appear inside a strong CO₂ gas absorption band centered at 4.3 μm that is saturated for the mean atmospheric pressures of Mars. In the absence of these clouds, the morphology of this band depends, for example, on the topography (surface pressure) and on local CO₂ fluorescence. In fact, CO₂ ice also absorbs in this area, but in contrast to the purely absorbing, deep CO₂ gas band, the ice absorption appears as a bright feature that can be seen inside the gas band. Resonant scattering of photons by the CO₂ cloud crystals appears as a spectral peak at 4.26 μm (Montmessin et al., 2007): this peak is the main signature we used for identifying the clouds. The second peak at 4.32 μm is, according to modeling by Montmessin et al. (2007)

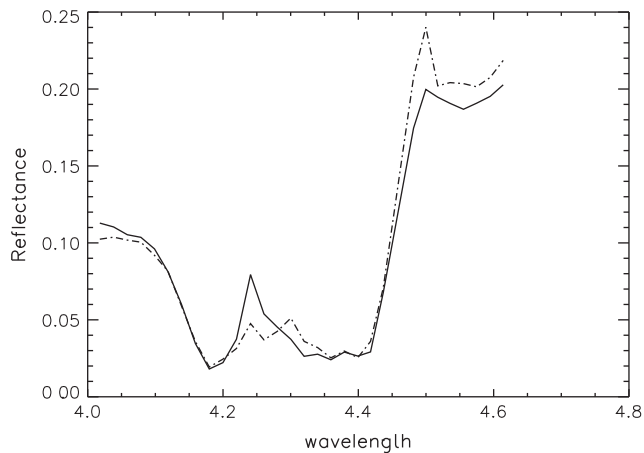


Fig. 1. Examples of OMEGA spectra with cloud detection: the solid line shows an occurrence of the first spectral peak at 4.26 μm inside the absorption band and the dash-dotted line shows a spectrum with the two peaks visible, the second at 4.32 μm .

with the SHDOM model (Spherical Harmonics Discrete Ordinate Method, Evans, 1998), related to optical depth and particle size. At 4.32 μm , the single-scattering albedo of CO_2 ice reaches a local maximum such that micron-sized particles scatter more efficiently than submicron-sized particles. This single-scattering albedo maximum may also introduce increased sensitivity to multiple scattering or high opacity conditions (e.g., for $\tau > 2$). However, observed optical depths of less than unity (see Section 3.4) suggest a primary sensitivity to particle size for the 4.32 μm feature.

We have treated the OMEGA nadir data with a detection method that defines the 3σ detection limit of the clouds in the 4.3 μm CO_2 absorption band. The goal of this method is to determine an objective detection limit for each observation and separate the signal of the clouds from the noise in a concise, statistically sound way.

If the density distribution of a certain I/F (reflectance) at the wavelength of detection of the CO_2 clouds is calculated ($dN/d(I/F)$ vs. I/F), the cloudless background noise distribution can be described as Gaussian, and the clouds can be seen as a second Gaussian mode with either clearly higher I/F values than the background

or then partly merged with the first, background Gaussian. This property of the data can be used to detect the clouds. The two panels of Fig. 2 illustrate this and the method for signal detection is explained below.

The general background level of the bottom of the 4.3 μm band has been calculated for every observational session (“cube”) separately, and consists of the thermal emission of the surface, possible fluorescence, and naturally the instrumental noise. This background level, “noise” for the detection, was assumed to be Gaussian, and its mean value and variance were calculated in an iterative process described below.

- First the mean and variance of each spectel (wavelength bin or spectral element) in the band were calculated for the whole image cube. However, at the cloud spectel (4.26 μm), the cloud signal causes a bias in the mean towards higher values of I/F . This affects the variance as well, in particular in the cases where the signal and the noise are of the same magnitude (the cloud Gaussian is “inside” the noise Gaussian, see Fig. 2b).
- Thus, assuming that the mean variance of the noise should be the same in the whole band, we calculated the average variance in the wavelength range (σ_{avg}) and used that also at the cloud wavelength (where the “local” variance (σ_{loc}) is larger because of the cloud signal).
- Then, using the calculated band average variance (σ_{avg}), we recalculated the local mean and local variance (σ_{loc}), but using only the data below $3\sigma_{\text{avg}}$ of the distribution: thus all the I/F values above $3\sigma_{\text{avg}}$ were left out of the recalculation of the new mean and variance.
- This process was repeated a number of times (10 was more than enough to converge) to acquire the true mean and variance of the Gaussian background “noise”, which were then used to map the 3σ detections of clouds in the wavelengths specific for these clouds (4.26 μm and 4.32 μm).
- To summarize, this method allowed for acquiring the true mean and variance of the noise also in the wavelengths where the cloud signal can affect them, and to detect the clouds at 3σ .

The 3σ limit should eliminate roughly 99% of the noise, but we have also conducted an additional noise canceling procedure by removing any spatially isolated pixels still remaining in the map after the 3σ analysis: this is based on assuming that a cloud should

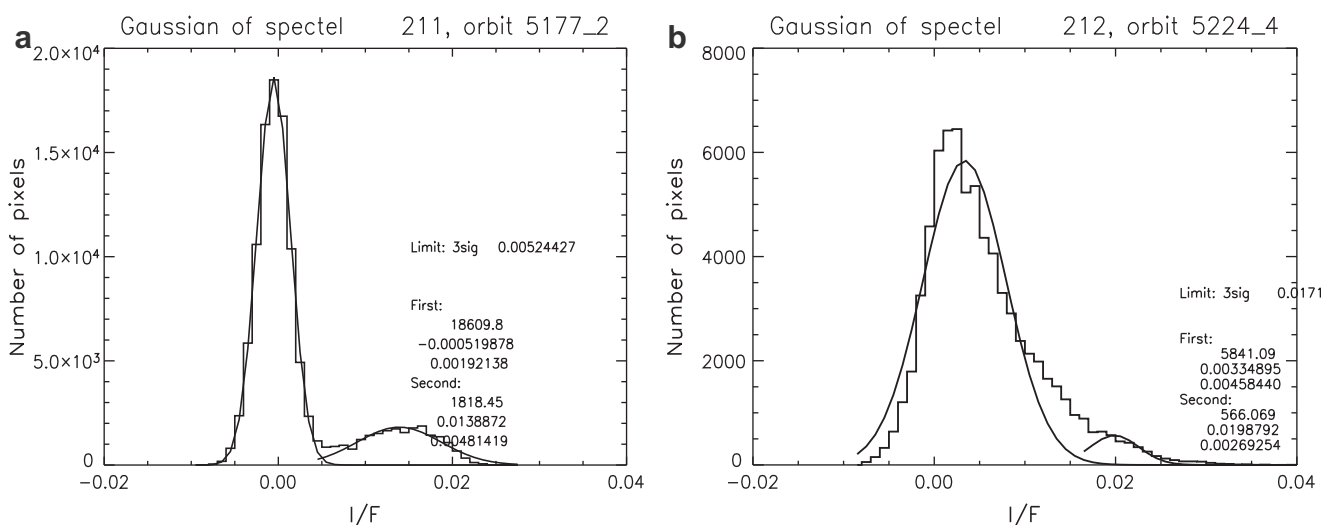


Fig. 2. Examples of the reflectance distribution at the cloud wavelength. The panel (a) shows a distribution with clearly separate noise and cloud Gaussians and both are also well fitted by a Gaussian curve. The panel (b) shows an example of an observation where the cloud is partly masked by the noise: the noise distribution deviates from normal towards higher values, indicating a presence of a signal, but a good fit is difficult to achieve.

Table 1

OMEGA CO₂ cloud observations during Mars Years 27 and 28. Note that the table is divided in two parts. Both parts include the following information: orbit and session number, median latitude of the cloud, median longitude of the cloud, local time (LT) and the solar longitude (L_s).

Orbit	Lat. °N	Lon. °E	LT	L_s	Orbit	Lat. °N	Lon. °E	LT	L_s
0314_2	−0.6	350.9	11.1	21.1	0967_6	−7.7	339.5	16.1	103.5
0430_2	−6.4	8.0	9.4	37.1	0997_6	9.3	270.9	15.7	107.3
0485_2	−1.4	2.6	9.0	44.0	1019_7	−17.4	269.8	15.5	110.1
0485_3	2.2	2.7	9.1	44.0	1041_6	−13.7	268.8	15.3	112.9
0501_2	−10.1	230.2	8.9	46.0	1055_6	1.3	332.5	15.1	114.7
0518_2	−9.4	356.1	8.5	48.1	1084_2	−1.8	2.9	14.8	118.5
0529_3	4.1	356.2	8.6	49.5	1103_5	−8.7	295.9	14.5	120.9
0551_3	1.0	353.4	8.4	52.2	1205_3	14.8	352.0	13.4	134.6
0551_4	5.8	353.0	8.5	52.2	1205_4	0.6	352.0	13.5	134.6
0567_0	−49.1	221.7	7.9	54.2	3000_6	3.3	12.1	16.9	51.6
0934_6	−4.9	341.4	16.4	99.3	3008_7	−15.3	307.1	16.9	52.6
0945_6	−3.8	340.4	16.3	100.7	4358_6	46.6	285.3	14.1	246.3

Table 2

OMEGA CO₂ cloud observations during MY 29. See Table 1 for details.

Orbit	Lat. °N	Lon. °E	LT	L_s	Orbit	Lat. °N	Lon. °E	LT	L_s
5062_4	−9.0	2.6	17.3	0.8	5225_3	−0.9	260.5	15.6	23.1
5080_4	0.4	7.5	17.1	3.3	5225_4	−16.1	260.3	15.7	23.1
5098_2	−2.9	7.1	16.9	5.8	5231_3	−1.1	19.7	15.5	23.9
5120_2	−1.5	325.4	16.6	8.9	5231_4	−6.4	19.7	15.7	23.9
5123_2	−0.5	25.1	16.6	9.3	5232_4	−6.5	279.9	15.7	24.1
5138_2	7.1	325.3	16.5	11.4	5239_3	1.9	299.8	15.5	25.0
5141_2	1.3	25.0	16.5	11.8	5239_4	−2.3	299.8	15.6	25.0
5146_2	−3.1	244.5	16.4	12.5	5242_3	9.9	359.3	15.4	25.4
5149_2	5.1	304.3	16.4	12.9	5242_4	−0.7	359.2	15.6	25.4
5170_2	−1.1	3.6	16.2	15.7	5257_3	3.7	298.4	15.3	27.4
5170_3	−16.6	3.5	16.3	15.7	5257_4	−0.8	298.3	15.4	27.4
5171_2	−1.0	263.2	16.1	15.9	5260_4	−0.3	358.1	15.4	27.8
5174_2	0.9	323.6	16.1	16.3	5267_3	6.4	17.3	15.1	28.7
5177_2	−5.3	23.1	16.1	16.7	5267_4	−0.8	17.2	15.3	28.7
5177_3	−13.4	23.1	16.3	16.7	5282_3	1.9	316.5	15.2	30.7
5203_3	−4.9	302.1	15.9	20.2	5285_3	0.1	16.1	15.1	31.0
5206_3	5.6	1.5	15.8	20.6	5321_3	−4.4	13.9	14.7	35.7
5212_3	−9.8	121.2	15.9	21.4	5321_4	−14.1	13.9	14.9	35.7
5224_3	2.7	0.7	15.6	23.0	5728_4	1.9	324.9	10.6	86.7
5224_4	−11.2	0.5	15.8	23.0	7254_0	−2.0	7.75	16.0	329.4

appear as a fairly uniform object and thus any cloud pixel should be in contact with at least one other cloud pixel. We also make sure that we remove no more than 1% of the pixels with this method (the amount of noise that remains still above the 3σ detection limit).

It should be noted that in this study we have limited the cloud detections with 3σ , but it is possible that faintest clouds remain unobserved. A search for clouds between 2 and 3σ will be left to a future study. However, their detection will be more difficult because of added contribution of noise.

The second peak (at $4.32\ \mu\text{m}$, related to cloud particle size, as explained above) has been detected and mapped with the same method as the first one, providing maps of its appearance inside the bulk cloud (analysed from the first peak at $4.26\ \mu\text{m}$). We have also mapped the spectral ratio of the two cloud peaks $SR = R(4.32\ \mu\text{m})/R(4.26\ \mu\text{m})$. Montmessin et al. (2007) showed with SHDOM radiative transfer modeling that a high peak at $4.32\ \mu\text{m}$ ($SR > 1$) indicates clouds particle effective radii $r_{\text{eff}} > 1\ \mu\text{m}$ (see Fig. 7c in Montmessin et al. (2007)).

3.2. Global mapping of the clouds

We have selected the potential cloudy orbits with running the statistical method described above on every OMEGA nadir orbit recorded by the end of MY 29. In addition, we checked the method-selected orbits visually. We have strictly limited our observations to clear cloud-shaped observations where the adjacent spectels

are also showing correlation (normally the cloud is seen nearly as well at $4.28\ \mu\text{m}$ than at $4.26\ \mu\text{m}$). This has resulted in a list of 51 orbits (which adds up to 64 OMEGA sessions, since on some orbits the cloud was observed in two adjacent sessions): see Table 1 for Mars Years 27 and 28 and Table 2 for Mars Year 29.

On the listed orbits of confirmed cloud detection, the previously described mapping method has been used to produce maps of the clouds, such as the examples shown in Fig. 3, where the cloud peak intensities are plotted on a latitude–longitude grid.

Fig. 4 shows the spatial distribution of the clouds where the color of the points describes the season of detection (see figure caption). It can be seen that both the spatial and seasonal distribution of the clouds follow the same lines as reported by Montmessin et al. (2007) based on the first series of about 20 observations. In general the clouds appear after spring equinox ($L_s = 0^\circ$), disappear for the aphelion period $L_s = 60\text{--}90^\circ$ (with one exception at $L_s = 87^\circ$), reappear, and continue to form still for some time until later in the summer (see Fig. 5). These observations are well in agreement with the Mars Global Surveyor (MGS) observations from Mars Years 24–26 (Clancy et al., 2007), except that MGS observed more clouds above Tharsis and no clouds between 30 and 50°W . In the MGS data the clouds reappear later ($L_s = 110^\circ$) after the aphelion season than in the OMEGA and HRSC data, where we even have one observation at the summer solstice ($L_s = 87^\circ$). In the last months of Mars Year 29 OMEGA observed an equatorial CO₂ cloud at $L_s = 330^\circ$: such an early start of the CO₂ cloud season has never been observed before, but the global

Table 3

All high-altitude cloud observations by HRSC: Mars Years 27 and 28. Listed are the orbit number (and image number when applicable), if OMEGA observed clouds as well, the mean cloud height, cloud speed, and the latitude, longitude, local time and L_s of cloud observation. Note that negative cloud speed indicates movement (wind) from east to west. "Not meas." means that the cloud altitude or speed was not measurable.

Orbit	OMEGA	Cloud, h (km)	Cloud speed (m/s)	Lat. °N	Lon. °E	LT	L_s
567_0	X	53–62	5–42	–48.9	220.5	7.9	54.2
602		87.3	Not meas.	–11.0	10.5	7.2	58.5
724_9		59.7	Not meas.	–44.5	282.6	7.3	73.4
923		62.1	Not meas.	1.0	342.3	16.4	97.9
934	X	59	–107	–6.1	341.3	16.3	99.3
945	X	66.7	–58	0.6	340.3	16.2	100.7
1055	X	59.3	–86	1.1	332.8	15.1	114.7
2990		70.5	0–15	–9.5	275.4	17.0	50.4
3000	X	67.4	–15	3.3	12.1	16.9	51.6
3030		63.8	–30.0	–1.8	304.1	16.5	55.4

Table 4

As Table 3 but for Mars Year 29. See Table 3 for details.

Orbit	OMEGA	Cloud, h (km)	Cloud speed (m/s)	Lat. °N	Lon. °E	LT	L_s
5109		68.1	–68	2.4	347.2	16.8	7.4
5117		79.2	–63	0.8	265.9	16.7	8.5
5134		76.4	–73	11.9	4.8	16.5	10.8
5135		79.8	–93	2.1	265.0	16.5	11.0
5141	X	83.2	–66	7.1	24.8	16.5	11.8
5146	X	79.2	Not meas.	7.8	244.8	16.4	12.5
5149	X	75.3	Not meas.	3.7	304.6	16.3	12.9
5153		73.5	–78	–0.17	264.1	16.3	13.4
5159		71.1	Not meas.	–6.9	24.1	16.4	14.3
5167		76	–60	3.1	303.5	16.2	15.3
5170	X	Not meas.	Not meas.	10.0	3.6	16.2	15.7
5177	X	72	Not meas.	–10.2	23.5	16.3	16.7
5196		71	–60	–5.3	281.9	15.9	19.3
5201		69.7	–83	–1.2	142.0	15.9	19.9
5206	X	74.7	–90	5.4	1.7	15.9	20.6
5207		80.7	–85	6.8	261.7	15.8	20.7
5208		66.4	–68	–10.0	161.0	15.8	20.9
5279_1		77.8	–63	0.5	257.1	15.1	30.3

climate model LMD-MGCM predicts the beginning of the cloud season already at around this L_s (see Section 5). However, no other clouds were observed in the end of MY 29.

In addition, we have one case of a very bright cloud at 45°N and at $L_s = 250^\circ$, which seems to be very late in the autumn compared to the general seasonality of these clouds. THEMIS-VIS has observed a significant set of such high-altitude autumn clouds in the northern midlatitudes at twilight (Inada et al., 2007; McConnochie et al., 2009). For this particular cloud the OMEGA imaging enabled us to check the same location 3 sols before and after the cloud observation, but no CO₂ signature was found at these times, suggesting that the cloud developed and dissipated in less than 3 sols. Two southern midlatitude clouds (45–49°S) have been observed in the local autumn: the first (session #0567_0) was already reported by Montmessin et al. (2007) with OMEGA spectroscopy confirming this cloud to be CO₂ ice. We report here an observation of the same cloud (#0567_0) from HRSC, and an additional observation of a southern midlatitude cloud by HRSC (session #0724_9).

According to these observations we have reason to believe that these daytime high-altitude clouds can be divided in at least two classes: the equatorial spring/summer clouds and the midlatitude autumn clouds. The frequency of occurrence for the midlatitude clouds remains to be mapped in more detail, preventing us from drawing further conclusions on interhemispheric differences.

For interannual variations we face a problem within this dataset: Unfortunately the OMEGA global coverage (in latitude, longitude and L_s) is quite uneven within the three years of observations. The first and third years of observation (MY 27 and MY 29) show frequent cloud formation immediately after spring

equinox, but during the second year (MY 28) we seem to have very few (only three) CO₂ cloud observations. However, this is most probably an artefact of sparse observations at seasons and locations of expected cloud formation (Fig. 5). Any conclusions on the interannual variability of CO₂ cloud formation based on Mars Express data will need to wait for longer datasets with a more homogeneous coverage at the expected cloud seasons and locations. It should be noted that Clancy et al. (2007) presented their MY 24–26 dataset with no remark of interannual variations, so we presume that they did not observe any significant differences between their three martian years. We can anyhow state that our MY 27 and MY 29 cloud observations are very similar in seasonal, longitudinal and latitudinal distribution with those of Clancy et al. (2007).

Local time variations are difficult to detect, since the observation times are limited to the afternoon by the polar orbit. However, particularly OMEGA has some observations in the morning, around 8–11 LT, and one HRSC observation has been acquired at dawn at 7 LT. TES observations (Clancy et al., 2007) and SPICAM observations (Montmessin et al., 2006a) revealed the existence of CO₂ clouds in both daytime and nighttime atmosphere with differing properties. We show here that CO₂ clouds are observed also early in the morning, and we will return to this aspect in Sections 5 and 6.

3.3. Structure in the spectral signature of clouds: interpretation and mapping

Montmessin et al. (2007) explained the physical foundation of the formation of the two spectral peaks described above

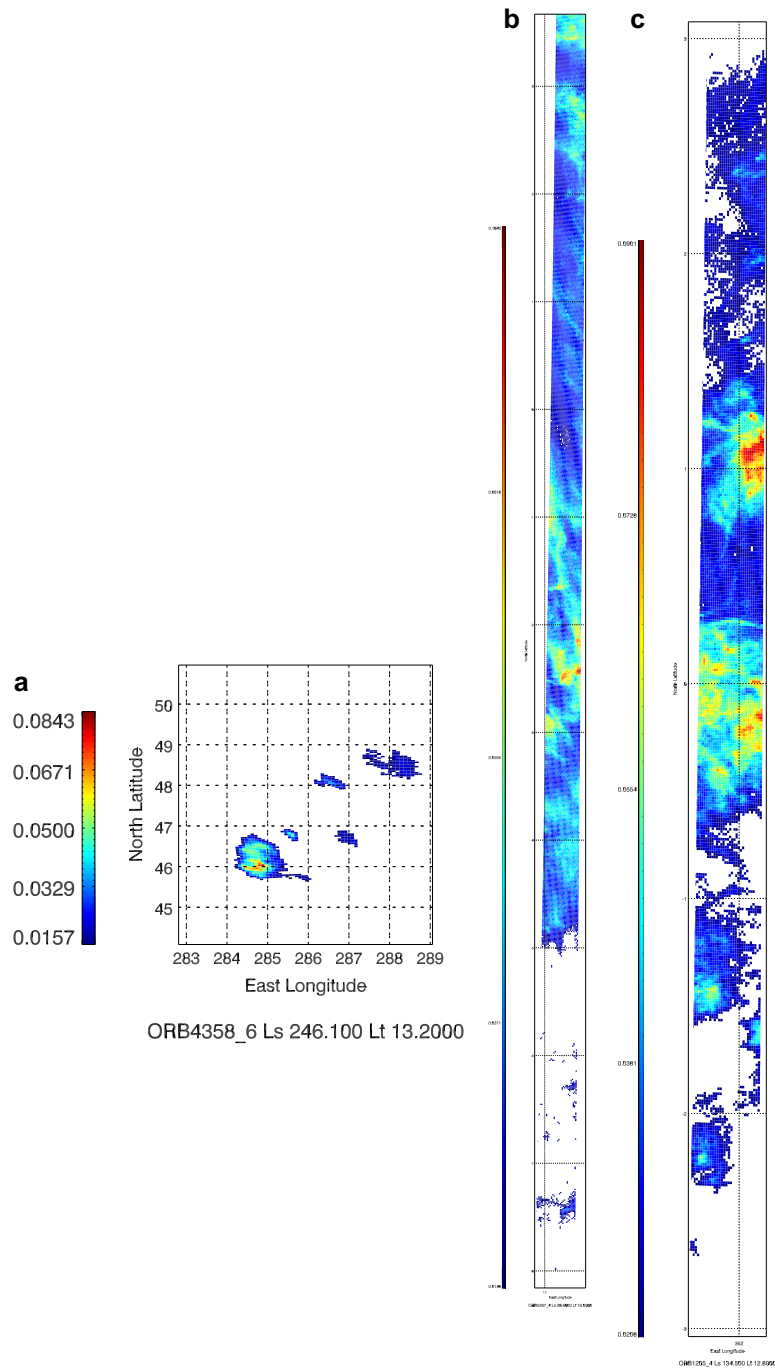


Fig. 3. Examples of the 3-sigma mapping of clouds with the intensity of the first cloud peak plotted over the martian surface. Panel (a) shows a very clear case of a clumpy, cumuliform-type cloud, panel (b) a more cirrus-type one, and panel (c) a cloud showing complex morphology.

(Section 3.1). We can relate the first peak ($4.26 \mu\text{m}$) to the occurrence of the clouds and the second ($4.32 \mu\text{m}$) mainly to the cloud particle size. The ratio of the peaks SR should tell us about the particle size: $SR > 1$ if the particle size exceeds $1 \mu\text{m}$ (Montmessin et al., 2007). Thus the variation of the ratio of the two peaks, SR , should give us information on the variation of the particle size. This hypothesis is used in the following.

We have mapped, using the method described in Section 3.1, the behavior of the two peaks and their spectral ratio on the 60 cloud occurrences registered during the first nearly three martian years of observations. The second peak ($4.32 \mu\text{m}$) is reliably observed (where the first and second peaks are correlated and cases

of isolated pixels are removed) in 63% of the cloud occurrences. Fifty-five percent of the clouds show at least some areas of the cloud exhibiting high values of SR ($SR > 1$), which means that in those cases the particle sizes in the cloud should exceed $1 \mu\text{m}$.

One case is shown in Fig. 3a for the mapping of the cloud area, and Fig. 6 for the spectral peak ratio SR variation. Fig. 6 shows that in most of the cloud area the second peak is weaker in intensity than the first peak ($SR < 1$), indicating particle sizes smaller than $1 \mu\text{m}$. However, high SR ratios can be observed in some concentrated areas of the cloud.

The SR ratio gives only qualitative information on the particle sizes. Fitting the cloud properties requires accurate radiative

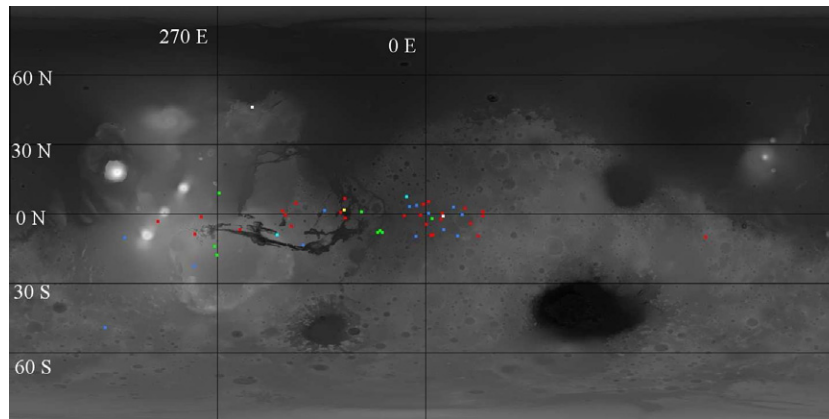


Fig. 4. Spatial map of OMEGA cloud observations. The positions of the 3-sigma detected clouds are plotted with colors. The colors depict different intervals of L_s : 0–30° in red, 30–60° in blue, 60–90° in yellow, 90–120° in green, 120–150° in cyan and $L_s > 150^\circ$ in white.

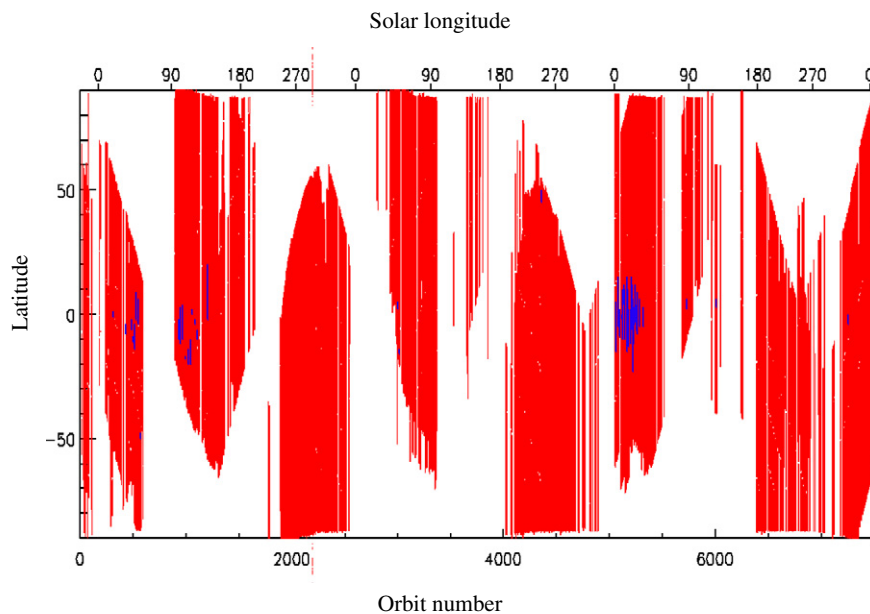


Fig. 5. Latitude-season distribution of the OMEGA nadir observations. The y-axis is the latitude and x-axis on top is the solar longitude L_s and below the orbit number. The blue lines show the locations of OMEGA CO₂ cloud observations acquired so far. It can be seen that the second year is particularly sparse in observations at the expected cloud formation locations and seasons.

transfer modeling of the behavior of the 4.3 μm band as well as the cloud spectrum within. Such modeling is not conducted here, but the SR ratio hypothesis can be tested with the particle radius analysis of two cloud shadow observations, explained in the following section.

3.4. Two cases of cloud shadow observation and analysis

As presented by Montmessin et al. (2007), cloud shadows were observed on two OMEGA orbits. These observations were used by Montmessin et al. (2007) to calculate the cloud altitude (≈ 80 km), the optical depth of the cloud ($\tau_c = 0.2$), and the effective radius of the cloud particles (1.5 μm) as averaged over the full cloud extent. However, the same analysis can be conducted pixel-by-pixel to provide detailed mapping of the cloud properties, which is described below.

The aforementioned cloud properties, the optical depth and the effective particle radius, can be calculated from the contrast ratio

of the reflectances inside and outside the shadow, i.e. the observed light extinction caused by the cloud. Normally, simple geometry should be used to relate cloud pixels with their corresponding shadow pixels. However, here we used another, very robust method. The analysed cloud area, defined by the mapping of the first cloud peak, can be used to define the boundaries of the cloud, and thus help to find the shadow pixels. The area of the shadow corresponding to the cloud was found by using the analysed cloud pixels as a mask, and finding the largest anticorrelation between the visible images of the shadow and the analysed 4.26 μm feature map (deepest shadow corresponds to the most intense cloud scattering). The shadow pixels were found this way, after which the contrast ratio was calculated. For the contrast ratio calculation the reflectance needs to be corrected for atmospheric effects to isolate the surface albedo component, and this was done by using a standard atmospheric correction procedure for OMEGA by Y. Langevin (personal communication, 2007). To calculate the contrast, a reference surface albedo spectrum outside the shadow is needed, and

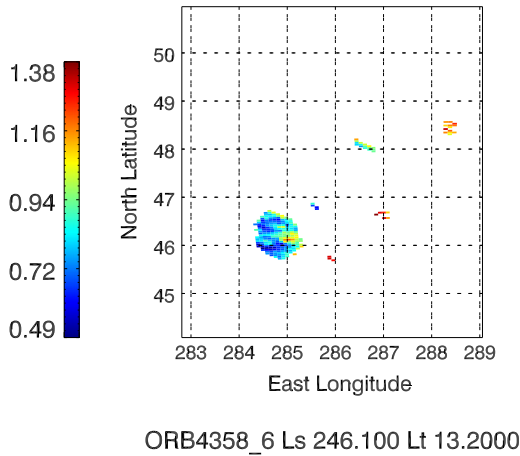


Fig. 6. An example of mapping of the variation of the spectral peak ratio SR . The plot shows the ratio of second and first peak intensities. If the value is higher than unity, the second peak exceeds the first peak intensity, which points to particles sizes larger than $1 \mu\text{m}$. The entire cloud can be seen in Fig. 3a.

this reference was found by averaging the reflectance of a 20×20 pixel area outside the shadow. Here we have assumed that the surface albedo does not change between the shadow and reference albedo areas.

Next we calculated the contrast ratio as a function of wavelength in the range $1.0\text{--}2.7 \mu\text{m}$ for each pixel, and any remaining large atmospheric absorption bands ($2.0 \mu\text{m}$ CO_2 gas absorption band) were removed for the effective radius analysis by excluding the corresponding wavelengths. This should not affect the acquired r_{eff} results but help in finding the best overall fit to the contrast ratio curve.

The optical depth of the cloud, τ_c can be calculated from the following relationship as described in Montmessin et al. (2007):

$$\frac{R_{\text{ish}}}{R_{\text{osh}}} = \frac{\exp[-\tau_c / \cos \theta] + \frac{F_{\text{dif}}}{F_{\text{dir}}}}{1 + \frac{F_{\text{dif}}}{F_{\text{dir}}}} \quad (1)$$

In Eq. (1) the R_{ish} is the reflectance of the surface inside the shadow and R_{osh} the equivalent outside of it, $\cos \theta$ is the cosine of the solar zenith angle and $\frac{F_{\text{dif}}}{F_{\text{dir}}}$ is the ratio of the diffuse and direct components of the solar flux outside the shadow, assumed to be controlled solely by atmospheric dust. Montmessin et al. (2007) estimated the $\frac{F_{\text{dif}}}{F_{\text{dir}}}$ to be about 0.3 with the SHDOM model (Evans, 1998) by using a moderate background dust optical depth of $\tau_{\text{dust}} = 0.2$. This dust optical depth value fits well the range of observations by the Mars Exploration Rovers (Smith et al., 2006) for the same season ($\tau_{\text{dust}} = 0.1\text{--}0.3$ with $L_s = 45\text{--}53^\circ$). We have estimated the possible error in evaluating the background optical depth. When $\tau_{\text{dust}} < 1$, an error of 0.1 in τ_{dust} will introduce a 10% error in the $F_{\text{dif}}/F_{\text{dir}}$. However, this leads into only 2% of error in the analysed optical depth of the cloud, which is negligible. It should be noted that in reality the cloud extinction influences the diffuse radiance, and this effect depends on the position in the cloud shadow (more pronounced in the center of the shadow). This can introduce a small bias in our analysis. However, the exact calculation of its effect requires 3-D radiative transfer modeling and here we settle for our simpler assumption. Eq. (1) can be solved for τ_c , which can be calculated for each observed cloud pixel using the contrast ratios calculated for each of the respective shadow pixels.

The cloud particle sizes can be estimated using Mie theory to calculate the optical properties of cloud crystals for size distributions of different effective radii r_{eff} , and then using these optical properties to calculate the theoretical cloud extinction, contrast ra-

tion, and its variation with wavelength, for the different effective radii r_{eff} . The optical properties were calculated for logarithmic size distributions of constant effective variance ($v_{\text{eff}} = 0.1$ and 0.2). The calculated cloud extinction was fitted to the observed contrast ratio using a Levenberg–Marquardt (L–M) method to find the best-fit r_{eff} for each pixel. See Montmessin et al. (2007) for details of the fitting procedure and their Fig. 10 for an example of a fit. We also used another method to verify the functioning of the L–M fitting routine: for every pixel, we simply calculated the χ^2 of the fit of observed and modeled spectra for effective radii in the range $0.1\text{--}10.0 \mu\text{m}$ with $0.1 \mu\text{m}$ intervals. As the end result we chose the r_{eff} with the best χ^2 produced by one of these methods. For most of the pixels the two methods agreed very closely, but quite many cases of ambiguous fits were acquired for the smaller effective variance $v_{\text{eff}} = 0.1$. With $v_{\text{eff}} = 0.2$ the fits are less ambiguous and the size distributions are unimodal: thus we are presenting here the results for analysis with $v_{\text{eff}} = 0.2$. The error bars used for the fit were calculated with the statistical readout noise of OMEGA (2 Digital Numbers), since the method is “auto-calibrating” in the sense that we use spectral ratios. This gave a 1σ error of about 0.2% on average for the contrast ratio. For fitting and calculating the χ^2 we used an average 3σ error of 0.6%.

The results of the shadow analyses for cloud optical depth and for cloud crystal effective radii are presented in Fig. 7a and c for orbit #0501_2 and in Fig. 7b and d for orbit #0551_3.

The optical depth of the cloud, τ_c , follows directly the shape and behavior of the shadow, as it should, and the maximum values of optical depth are around $\tau_c = 0.5\text{--}0.6$ with a mean and variance of 0.14 and 0.006 (median 0.13) for session #501_2, and 0.25 and 0.026 (median 0.20) for session #551_3. Our detection limit is estimated to be around $\tau = 0.01$.

Fig. 8a and b shows the size distributions of the analysed effective radii for the two orbits. As the histograms show, the effective radii are mainly confined between 1 and $3 \mu\text{m}$. The effective radii figures (Fig. 7c and d) have been limited to sizes smaller than $r_{\text{eff}} = 4.0 \mu\text{m}$ to show the spatial variations of the particle sizes in the bulk of the cloud: it should be noted here that most of the particles are in this limited size range. The fitting errors stayed mainly below 10% for the main mode of the particles ($1\text{--}3 \mu\text{m}$). However, we see reliably observed submicronic particles only in the orbit #0551_3 and their relative errors exceed 10%.

To reveal any possible correlations between the analysed cloud properties, we performed a correlation study between the effective radii and optical thickness. The effective radii are not correlated with optical depth (see Fig. 9a and b), even if in the orbit #0551_3 the particle radii seem to decrease for $\tau < 0.1$.

The effective radius analysis can be compared with the mapping of the second spectral peak of the clouds (at $4.32 \mu\text{m}$) that should be indicative of the particle size. We defined previously the ratio of the second ($4.32 \mu\text{m}$) and first ($4.26 \mu\text{m}$) as SR , and if $SR > 1$, the particle size should exceed $1 \mu\text{m}$. In a major part of these two clouds the second peak is, indeed, higher than the first (not shown), implying particles larger than $r_{\text{eff}} = 1.0 \mu\text{m}$. However, a correlation study (see Fig. 9c and d) for the two sessions #501_2 and #551_3 shows that there is no correlation between the peak ratios SR and the analysed r_{eff} , although in nearly all cases of $r_{\text{eff}} > 1.0 \mu\text{m}$, the peak ratios SR are also higher than unity. However, in the cases where the peak ratios SR are less than unity, the analysed effective radii stay above $1 \mu\text{m}$. In the few submicronic particle cases of session #0551_3 only one pixel shows $SR < 1$. According to this result the peak ratio cannot be solely used to analyse particle sizes: the changing thermal contribution from the surface, the topography, and possible fluorescence influence the CO_2 band depth as well. Without precise radiative transfer modeling and fitting of all the parameters (a future study), the

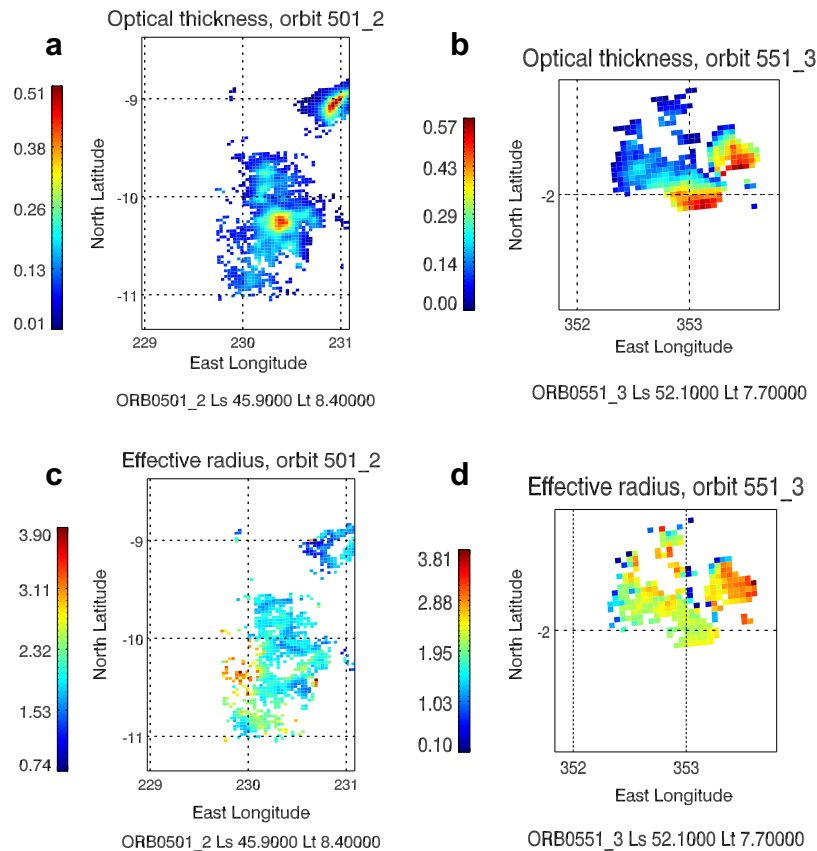


Fig. 7. The analysed opacity (τ) and cloud particle effective radii (r_{eff} in μm) from cloud shadow observations: (a) τ , #0501_2; (b) τ , #0551_3; (c) r_{eff} , #0501_2; (d) r_{eff} , #0551_3.

second peak height can only give us qualitative clues about the particles sizes, but not much quantitative information.

4. Results from analysis of HRSC images

Fig. 10a–g shows examples of HRSC cloud observations with analysed OMEGA cloud data at $4.26 \mu\text{m}$ superposed in mutual sessions (subplots a, b, d, and e). Fig. 10a exhibits two types of cloud morphology, a very diffuse, thin cloud in the upper part of the image (as does the lower part of Fig. 10d), and a more filamented, patchy cloud in the lower part. Fig. 10b instead shows a beautiful mutual observation of a filamented cloud. Fig. 10c is a special case of a morning cloud: the Sun is very low in the east (right) and clouds outside the image cast the very long shadows seen on the surface. The upper part of Fig. 10d shows an interesting structure where the cloud seems more concentrated at the edge of the valley formation of the top left corner, followed by a series of ripples emanating from the main cloud towards the lower right. Fig. 10e and f reveals complex morphologies showing tufts and aligned filaments. The last image, Fig. 10g, gives an example of a type of diffuse, patchy cloud observed by HRSC.

The results of the HRSC cloud altitude and wind speed observations are shown in Fig. 11a–d. Fig. 11a gives the overall picture of the seasonal and longitudinal distribution of the clouds. They are mainly confined on both sides of the main meridian with a slight preference for the western hemisphere. The cloud altitudes are found mainly in the range 50–70 km for MY 27–28 and 66–83 km for MY 29 (Fig. 11b). The overall altitude range of HRSC observations is larger than that observed by MGS (70–75 km, Clancy et al., 2007). Fig. 11b shows a hint of a trend for lower cloud altitudes in mid-spring and early summer as opposed to early spring.

However, this might be revealing an underlying interannual variation, since all the early spring observations are from MY 29. Assuming seasonal variation is the cause, the trend may result from a seasonal decrease of the cloud altitude between $L_s = 10^\circ$ and $L_s = 60^\circ$. However, Clancy et al. (2007) did not observe any clear seasonal altitude variations in their dataset, but they did note that the clouds of the northern hemisphere early fall period may present generally slightly lower altitudes. It is anyhow possible that the clouds form at roughly the same pressure level, and that it is the altitude of the pressure level, which varies with time (because of the thermal structure below the clouds). A significant decrease of the altitude of a given density level between $L_s = 10^\circ$ and $L_s = 60^\circ$ is observed in the SPICAM stellar occultation dataset (see Fig. 4, Forget et al., 1999). Fig. 11c shows the cloud altitude as a function of latitude: even if the two points that correspond to the special case of the orbit #0567_0 at 50°S latitude are excluded, it seems that the cloud altitudes north of the equator are higher than south of the equator. There again, this may be partly explained by variations of the atmospheric thermal structure below the clouds rather than changes in the cloud pressure level as suggested by SPICAM stellar occultation data (see Fig. 14a, Forget et al., 2009). No other trends were found in the altitude data.

The observed wind speeds vary a lot in the range of 5–107 m/s (Fig. 11d) dominated by easterly winds with only one case of westerly winds (session #0567_0) at southern midlatitudes. In this one special case during MY 27 the cloud altitude was observed to increase towards the south pole from 53 to 62 km within about 7° of latitude ($46\text{--}53^\circ\text{S}$). This cloud has so far been also the farthest CO_2 cloud observation away from the equator. Furthermore, the wind speeds measured are in the range of $\sim 5\text{--}42$ m/s in a prograde direction from west to east (as expected for prevailing winds in the midlatitudes), and not from east to west, as for the equatorial cloud

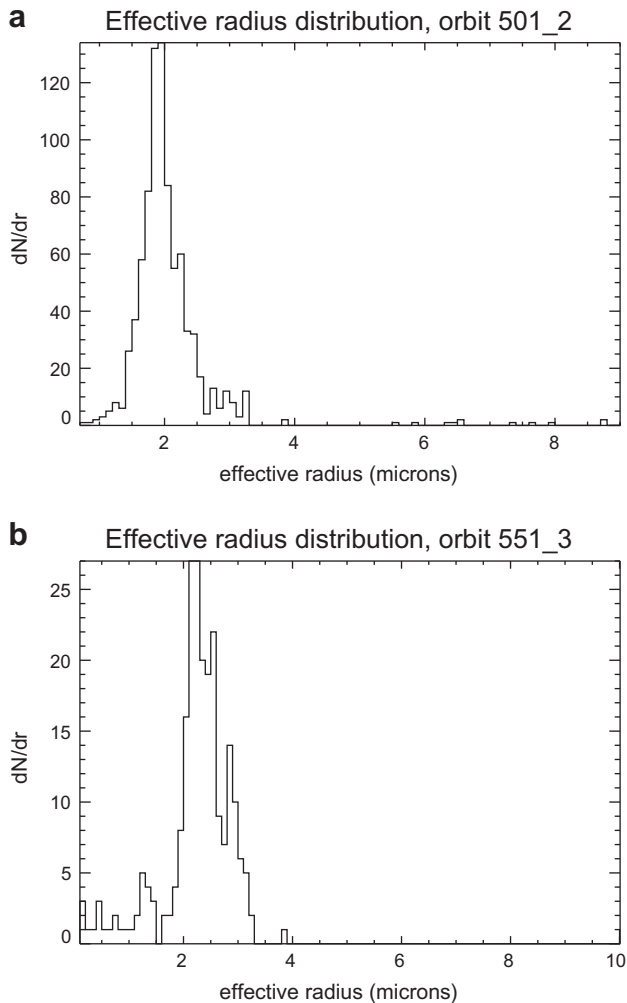


Fig. 8. The size distributions of the analysed cloud particle effective radii (in μm) for orbit (a) #501_2 and (b) #551_3.

observations. No strong general trends were found in the winds. It should be noted anyhow that atmospheric (stationary and propagating) waves can affect the observed cloud speeds, but near the equator most probably the fairly strong easterly zonal winds dominate the overall cloud speeds. This will be looked more into in the next section.

5. The mesospheric structure in the LMD-MGCM

We have used the LMD Mars General Circulation Model (LMD-MGCM) to study the structure of the mesosphere, in particular, at the seasons and locations of mesospheric cloud formation. The LMD-MGCM that originally had an upper limit at about 80 km (Forget et al., 1999) solves the primitive equations of hydrodynamics on a sphere, using a grid point discretization. The radiative balance accounts for the effect of CO_2 and suspended dust. A realistic CO_2 condensation scheme is included, essential for a good simulation of the surface pressure annual cycle. A water cycle (Montmessin et al., 2004) and a photochemical model for the lower atmosphere (Lefèvre et al., 2004) have also been included in the model. A number of subgrid-scale processes near the surface are considered, in particular the boundary layer turbulence, convection, relief drag and gravity wave drag. The LMD-MGCM has been extended to the thermosphere, becoming a ground-to-exosphere GCM. For this purpose, parameterizations for the physical pro-

cesses specific of the upper atmosphere have been included. The model takes into account now the energetic processes that determine the thermal state of the martian upper atmosphere: NLTE corrections to the NIR radiative transfer, heating due to the absorption of UV solar radiation and thermal conduction. The concentration of the different species is traced using a photochemical model adapted to the conditions of the upper atmosphere and a parameterization of the molecular diffusion. More details can be found in Angelats i Coll et al. (2004, 2005) and González-Galindo et al. (2009).

The LMD-MGCM was run, using the usual 64 (lon.) \times 48 (lat.) \times 50 (vertical) grid, for the season of most abundant cloud observations, $L_s = 0$ – 60° and the model fields were studied in particular in the altitude (60–90 km) and latitude (30°S – 30°N) range of cloud observations.

Montmessin et al. (2007) reported that the daily average mesospheric temperatures in the LMD-MGCM did not allow for CO_2 condensation, even if the distribution of the modeled temperature minima corresponded well to the distribution of the cloud observations. It has been recently described by observations and models (Lee et al., 2009; González-Galindo et al., 2009) that these altitudes experience large diurnal temperature variations caused by the propagation of thermal tides. A detailed inspection of the model climatology in the middle atmosphere shows that at the altitudes that present a minimum of temperature at, for example, 4 pm, 12 h later the temperature is maximum, and vice versa (see Fig. 12a and b). This daily variation could not be seen in Fig. 12 of Montmessin et al. (2007), since they presented a daily average temperature field.

Even though we focus on the period $L_s = 0$ – 60° in the following, it should be noted that the MGCM predicts well the temperature minima associated to the cloud observation locations and seasons during the whole year. It also predicts the start of the cloud season (minimum temperatures) already at $L_s = 330^\circ$ (OMEGA session #7254_0).

Most of OMEGA, HRSC and TES cloud observations have been made in the afternoon, and the clouds have been observed between 60 and 85 km, in good agreement with the altitude of the minimum of temperature predicted by the LMD-MGCM at this local time (Fig. 12a). Note also that the model predicts very cold temperatures during the night at about 100 km, in good agreement with the altitude of the nighttime clouds observed by SPICAM (Montmessin et al., 2006a). However, some clouds have been observed early in the morning, and these cases would require a more detailed comparison with the model. The coldest regions predicted by the model are also longitudinally confined to the same region as the cloud observations. The average temperatures for the $L_s = 0$ – 30 season in the model do not reach saturation, but are between 10 and 15 K above it for the conditions of OMEGA observations. When looking at the instantaneous (not time-averaged) profiles (Fig. 12c), some of them show temperatures only some degrees above CO_2 condensation temperature, but still no profile goes below condensation.

Comparisons with SPICAM temperature profiles showing that the temperature can decrease significantly below the condensation temperature of CO_2 (Montmessin et al., 2006b) imply that the LMD-MGCM tends to overestimate the temperatures in the upper mesosphere–lower thermosphere region (Forget et al., 2009; González-Galindo et al., 2009). Forget et al. (2009) and González-Galindo et al. (2009) suggested that this discrepancy between the model mesosphere and the observed one is a consequence of the IR radiative balance calculation in the model. The $15\ \mu\text{m}$ cooling parameterization uses an internal simplification of a constant and uniform atomic oxygen profile instead of using the one calculated by the GCM. Too low oxygen leads to less efficient cooling and overestimated temperatures.

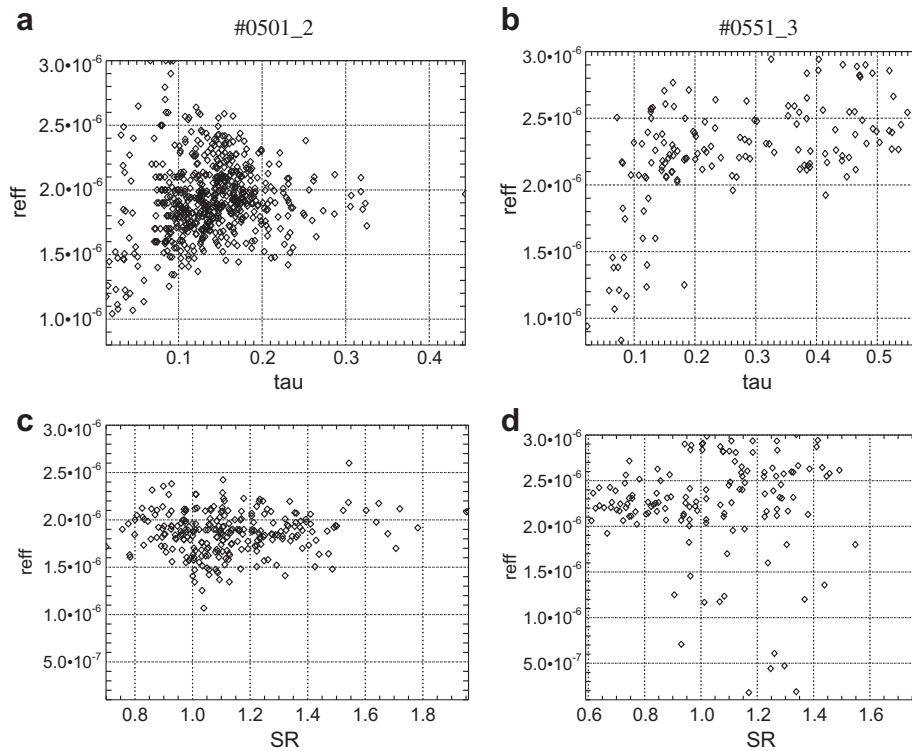


Fig. 9. The scatterplots of the analysed cloud particle effective radii (in m) versus the cloud opacity (at $1\ \mu\text{m}$) for orbit #501_2 (a) and #551_3 (b). The scatterplots of the analysed cloud particle effective radii (in m) versus the ratio of the two cloud spectral peaks SR ($4.32\ \mu\text{m}$ over $4.26\ \mu\text{m}$) for orbit #501_2 (c) and #551_3 (d). The ordinate range has been limited to sizes less than $3\ \mu\text{m}$ since most of the points lie in this range.

Is this underestimation of the $15\ \mu\text{m}$ cooling preventing the LMD-MGCM to predict subcondensation temperatures at the altitude range where the CO_2 clouds have been observed? We have performed some tests using the model-calculated atomic oxygen profile in the $15\ \mu\text{m}$ cooling parameterization. These tests show a decrease of the simulated temperature, and so an improved fit with the SPICAM observed profiles, only above about $100\ \text{km}$. The temperature at the altitudes where the CO_2 clouds are observed ($60\text{--}85\ \text{km}$) remained almost unaltered.

This might imply that other deficiencies in the thermal balance of the mesosphere are preventing the model to predict subcondensation temperatures. Given that the main heating term at these altitudes is the CO_2 NIR heating (Bougher et al., 1999), it is possible that an overestimation of this heating term, probably linked to uncertainties in the NLTE modeling, might be producing an overestimation of temperature. Other factors, such as problems in the propagation of waves from the lower atmosphere and its interaction with the in situ generated tides, or in the effects of the dynamics over the temperatures, might also have an effect.

However, Fig. 12c shows that some of the individual temperature profiles are only a few degrees above condensation, meaning that with a small perturbation the temperatures can reach and go below the saturation. The GCM grid is much larger than the typical scale of these CO_2 clouds: some subgrid-scale processes, like gravity waves, might provide this temperature perturbation in some points. In the terrestrial case, it has been shown (Noel et al., 2009) that strong small-scale temperature fluctuations produced by gravity waves trigger the formation of certain types of polar stratospheric clouds. In that terrestrial study, GCM modeling predicts minimum temperatures where clouds are observed, but is not able to predict temperatures low enough for these clouds to form. Noel et al. (2009) show that mesoscale modeling is needed to resolve gravity waves and predict temperature perturbations

leading to profiles below condensation in specific locations. Using GCMs is very helpful to identify the mesospheric areas with lower temperatures and thus higher possibilities of producing CO_2 clouds (further comparisons between the LMD-MGCM predicted temperatures and the location of CO_2 clouds will be published elsewhere). It is clear that a necessary further step is to carry out mesoscale modeling to study mesospheric CO_2 clouds: on the one hand, the meteorological context and possible origin of the clouds, and on the other hand, the atmospheric dynamics involved in shaping the clouds, should these be convective processes or not.

Also the wind fields in the mesosphere and the HRSC cloud speed observations were compared. The predicted zonal winds exhibit strong variations even in the monthly averaged plot at $80\ \text{km}$ altitude at the equator in Fig. 13a, where also the winds inferred from cloud observations of the HRSC are plotted with crosses. The solid line is the zonal wind speed monthly average and the dashed lines give the standard deviations, and negative values indicate easterly winds. The LMD-MGCM predictions fit remarkably well with the HRSC observations, except for three measurements at about 100°W . We looked at the individual profiles at this longitude (Fig. 13b) and discovered that the model profiles exhibit large diurnal variations and the predicted easterly wind does attain speeds up to $100\ \text{m/s}$ in the altitude range of $60\text{--}90\ \text{km}$. It should be noted that we chose near-equatorial HRSC observations for the comparison, but they come from different altitudes in the range of $66\text{--}81\ \text{km}$. However, the MGCM wind vertical structure is quite constant in this altitude range, which can also be seen in Fig. 13b.

In conclusion we can say that the comparison between the model and the observations has turned out fruitful: the model predicts the coldest temperatures at the locations and times of the cloud observations, and the predicted wind speeds coincide well with the observed cloud speeds. However, supersaturation is not

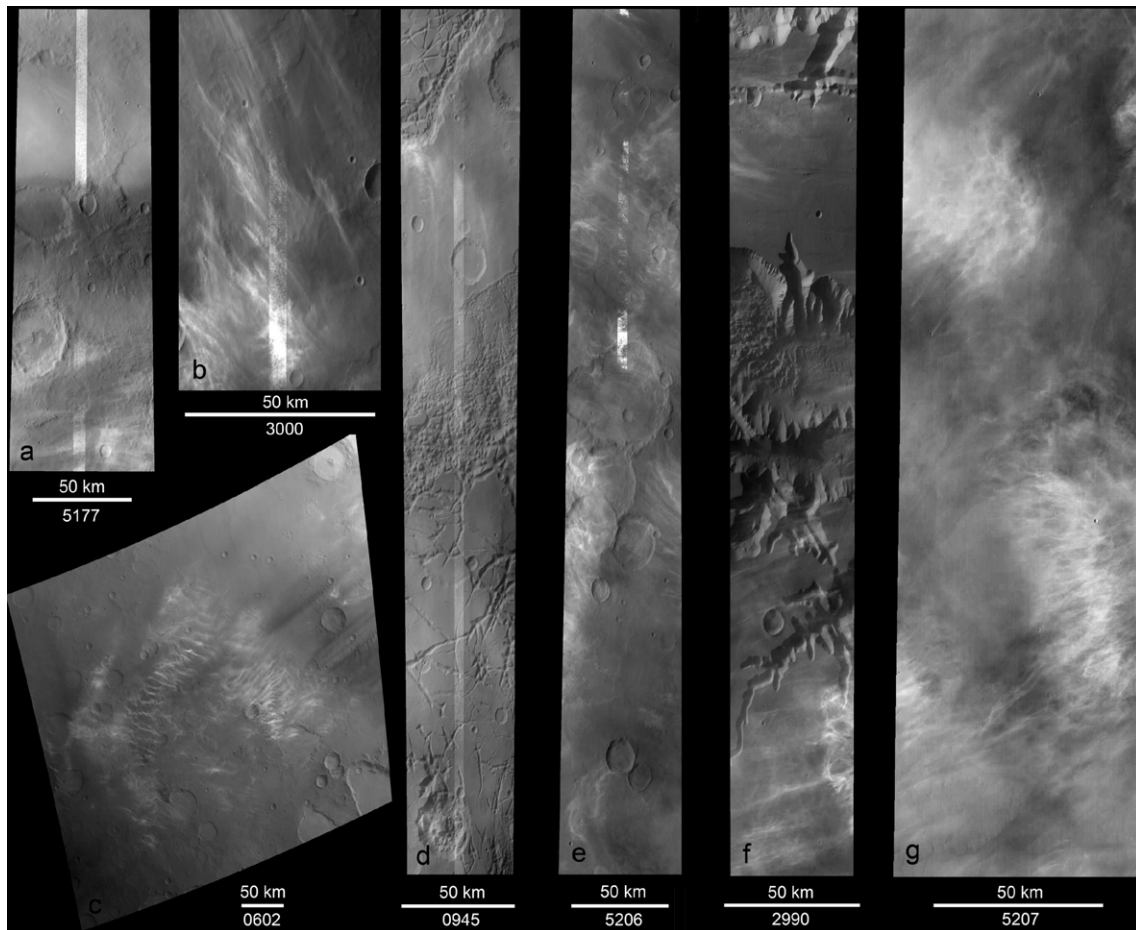


Fig. 10. Examples of HRSC high-altitude cloud observations. Images a, b, d, and e show also the corresponding analysed OMEGA clouds superposed (the narrower image strip). See Tables 3 and 4 for details of the observations. The image 0602 (c) shows an example of morning clouds with a local time of 7.2 h. Sun is from the right (east) with very low elevation revealing very long shadows of clouds further in the east. The other images were acquired in the afternoon with local times 16 and 17.

reached in the model, revealing a caveat in the model processes. The CO₂ cloud observations from different instruments provide a rare, growing dataset on the mesosphere of Mars giving new constraints to atmospheric models that will enable improvements of modeling of the middle atmosphere. We will conduct a detailed comparison of all available CO₂ cloud datasets and the LMD-MGCM in a future study.

6. The morphology of the clouds: cumulonimbus and cirrus types

6.1. Observations

The clouds observed by OMEGA and HRSC exhibit a variety of forms, but two main types can be established from the observations. It has to be noted, though, that the width of the OMEGA and HRSC tracks varies, depending on the distance between the planet and the satellite. The OMEGA track can be very narrow, in which case any interpretation on the cloud structure leads to significant, no matter how educated, guessing. However, when possible, combining the OMEGA image with the wider HRSC image having a swath width of 11.9° more details on the cloud morphology can be distinguished. When OMEGA observes far from the pericenter, it can also see larger structures in the consequently wider images.

Most of the observed clouds are clearly cirrus-type, filamented structures occasionally organized in what seems to be consecutive

waves (in HRSC images in particular) or less organized features. In 15% of the OMEGA observations (9 cases) the clouds are seen as rather round, clumpy masses. For the remaining 85% it should be noted that the OMEGA track width limits the interpretation and saying that all the 85% is cirrus-type would most probably lead to an overestimation of this number. Examples of different OMEGA cloud types are presented in the panels of Fig. 3. Most of the clumpy cases were already reported by Montmessin et al. (2007) and based on these observations they evoked the idea of these clouds being the result of mesospheric convection on Mars.

However, in the HRSC observations the clouds are dominated by a cirrus-type morphology, supporting the predominance of this type of clouds. There are some HRSC observations of different types of patchy or diffuse clouds, such as Fig. 10d, e, and g.

The 9 OMEGA cases of clumpy, cumuliform clouds have been acquired when OMEGA was observing far from the pericenter and from the surface, yielding image widths of several degrees. Eight observations were made in the morning, between local times 8–11, and one (the autumn midlatitude cloud of #4358_6 at 50°N) at 14 LT. Related to the local times of these observations of the clumpy, cumuliform clouds, it should be pointed out that the limited observation timeframes of polar orbit satellites (often LT 14–18) may inhibit the discovery of different morphologies in datasets. However, if we consider these observations with the mesospheric temperatures of the LMD-MGCM (Section 5), the convective hypothesis seems rather unintuitive: why would we observe strong convection during the warm morning hours at the cloud

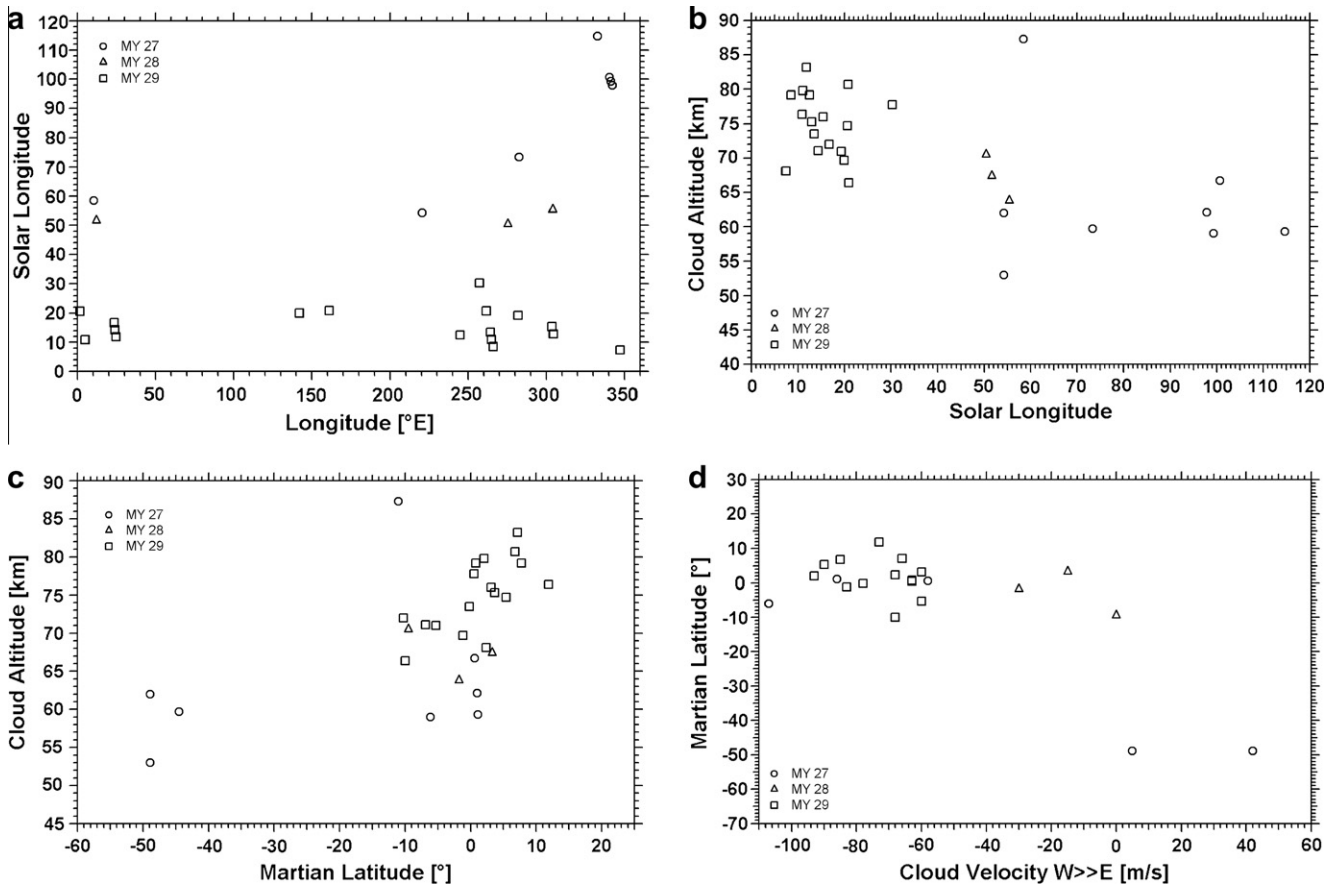


Fig. 11. HRSC mesospheric CO₂ cloud observations in Mars Years 27–29: (a) solar longitude versus longitude; (b) cloud altitude versus solar longitude; (c) cloud altitude versus latitude; (d) cloud latitude versus cloud speed. Note that the orbit #0567_0 is marked with two circles since it exhibits large variations in cloud altitude and speed.

formation altitudes, but not in the afternoon when the temperatures are the coldest (and expected supersaturations the highest)?

We will examine here the mesospheric convection hypothesis of Montmessin et al. (2007) with the help of theory and the few observational constraints we have.

6.2. Possible interpretations

Presuming that the clumpy clouds are a result of mesospheric convection, we present two (out of many) possible hypotheses.

In light of the moist convection hypothesis presented by Montmessin et al. (2007), these two cloud types could be related to different phases in cloud development. On the Earth, the convective clouds have quite limited lifetimes despite their vigorous nature: when convection ceases, the round, cumuliform cloud mass transforms into a filamented structure, when the upper part of the cloud, the anvil composed of ice crystals, detaches from the lower part that dissipates by end of convection and rainout. In fact, we might be seeing these two stages in the OMEGA observations. This hypothesis leads to the following explanation: The cases when we have caught the cumuliform structure, the cloud is fairly young and convection is still fueling the growth of the ice particles and the vertical velocities that keep the particles lofted. The observations showing more cirrus-type clouds could be related to the old age of the cloud, the phase of dissipation, when we are only seeing the remnants of the ‘anvil’ cloud top composed of smaller particles, whereas the larger particles have already sedimented out and evaporated in the subsaturated layers below. It should be noted that in the case of Mars the anvil and the bulk cloud are both formed of ice crystals, whereas on Earth the anvil is the

frozen top of a cloud formed of liquid droplets. Some HRSC images seem to show behavior where the two stages of cloud development may be visible (see the upper part of Fig. 10d).

Another hypothesis is that these two types of clouds would form in different conditions and through different nucleation pathways (homogeneous vs. heterogeneous). Different nucleation pathways require different initial supersaturations, and the supersaturation at cloud formation defines also the potential for growth of the cloud (through the latent heat of condensation and the so-called CAPE, defined and discussed later).

Previously, heterogeneous nucleation has been deemed the only realistic pathway for ice crystal formation on Mars, since the condensation nuclei (CN, dust grains) are so abundant and since homogeneous nucleation requires so high critical saturation ratios (Wood, 1999; Colaprete and Toon, 2002, 2003; Määttänen et al., 2005). However, in conditions lacking dust to initiate the heterogeneous nucleation process, the atmosphere might get very highly supersaturated. This could happen high in the atmosphere, which is easily depleted of dust since the sedimentation velocities of dust grains are very large in the thin atmosphere of Mars. In addition, the classical nucleation theory shows a temperature dependence, where in lower temperatures a higher saturation ratio is required for nucleation (Pruppacher and Klett, 1997; Vehkamäki, 2006). This means that higher in the atmosphere, where (assuming a standard lapse rate) temperatures are lower, nucleation requires higher saturation ratios than near the surface: thus we can expect to find highly supersaturated ‘cold pockets’ high in the martian atmosphere. Actually, very high supersaturations have been observed by SPICAM on MEx (Montmessin et al., 2006b; Forget et al., 2009). Thus, if the atmosphere cools and the supersaturation

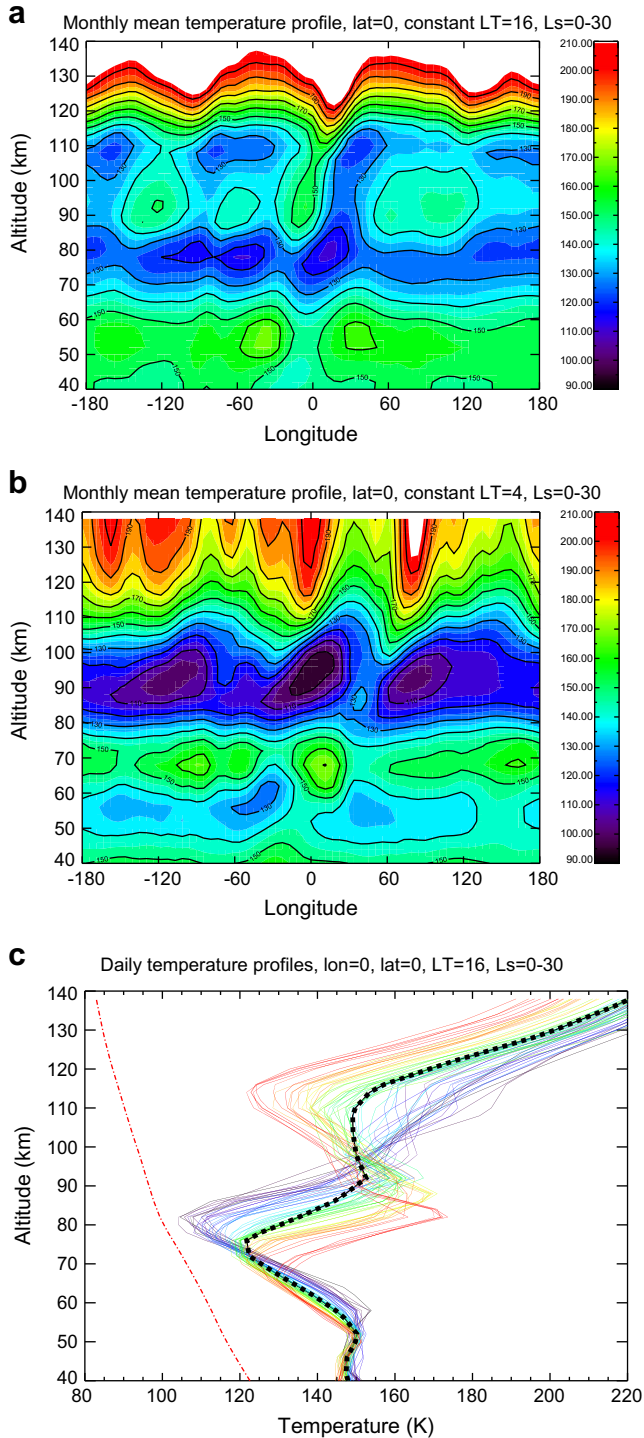


Fig. 12. The GCM temperature altitude–longitude cross-sections at the equator for the season $L_s = 0\text{--}30^\circ$ for two local times, (a) LT 16 and (b) LT 04. (c) The individual temperature profiles from the GCM temperatures at the equator and prime meridian for the season $L_s = 0\text{--}30^\circ$ for the local time (LT 16) and the coldest temperatures at cloud altitudes. The black dashed line represents the monthly-averaged temperature. The red dash-dotted line is the condensation temperature of CO_2 .

increases enough, perhaps homogeneous nucleation might happen in the lack of condensation nuclei.

Estimates of required supersaturations and temperature deviations for the different nucleation pathways can be calculated with the help of nucleation modeling. We have used the model of Määttä et al. (2005) and Vehkamäki et al. (2007) to estimate

some values. Homogeneous nucleation of CO_2 at ≈ 80 km altitude (pressure 10^{-2} Pa) requires extremely high saturation ratios ($S_{\text{nuc1}})$ and large temperature deviations (ΔT) from saturation ($S_{\text{nuc1}} \approx 10^{15}$, $\Delta T \approx 50$ K) as already predicted by Määttä et al. (2005) for near-surface conditions. Heterogeneous nucleation was investigated with nanometer scale condensation nuclei ($R_{\text{CN}} = 1$ nm) to get an upper limit of the required saturation ratios: $S_{\text{nuc1}} \approx 300$, $\Delta T \approx 15$ K. The required temperature deviations from saturation are clearly larger for homogeneous nucleation, even though they are quite large for both cases high in the atmosphere, in particular with small CN for heterogeneous nucleation. It should also be noted that the ΔT for homogeneous nucleation implies atmospheric temperatures of the order of 50 K, which is an extremely low value that has never been observed in the martian atmosphere.

The Convective Available Potential Energy (CAPE) describes the kinetic energy (buoyancy) a statically unstable air parcel can maximally acquire (Holton, 1992). It is defined as

$$\text{CAPE} = \int_{z_{\text{LFC}}}^{z_{\text{LNB}}} g \left(\frac{T_{\text{parcel}} - T_{\text{env}}}{T_{\text{env}}} \right) dz = \frac{w_{\text{max}}^2}{2} \quad (2)$$

where z_{LFC} is the level of free convection, z_{LNB} the level of neutral buoyancy, g the gravitational acceleration, T_{parcel} the air parcel temperature, T_{env} the temperature of the environment and w_{max} the maximal vertical velocity the statically unstable air parcel might reach. In a potentially (conditionally) unstable situation the latent heat released by condensation can lead to liberation of the CAPE, initiating and fueling strong convection. The CAPE is particularly large in highly supersaturated situations, where environment is very cold and the air parcels warmed by the latent heat in condensation become clearly warmer than their surroundings, and thus buoyant. Thus the vigorous convection could be initiated by homogeneous nucleation leading to a large CAPE and release of latent heat since the deviation from saturated state (very large in this case) defines the amount of energy released for convection. In the case of available condensation nuclei, heterogeneous nucleation (even on nano-size CN) requires much lower supersaturations than homogeneous nucleation, implying smaller CAPE, releasing less energy and leading to shallower convection and different type of clouds.

In summary, the two possible interpretations presented here for the formation of the two types of clouds are: (1) we are observing two different stages of the cloud life cycle, the convective clouds representing young and mature clouds and cirrus-type clouds the dissipating old clouds, or (2) there are two different pathways for cloud formation, when the convective clouds would form by homogeneous nucleation releasing more CAPE and the cirrus-type by heterogeneous nucleation leading to weaker updrafts.

These two possible hypotheses on the disparity in the cloud morphology presented here will be tested in a future work in cloud and atmospheric fine-scale modeling. We nevertheless propose in what follows a preliminary discussion on the likelihood of CO_2 convective structures, based on first-order theoretical CAPE calculations. We will also compare the evaluated CAPE values and the temperature deviations for different nucleation pathways.

6.3. Mesospheric cumulus clouds and CAPE

In the case of polar CO_2 clouds, Colaprete et al. (2008) estimated the martian CAPE from Radio Science measurements and general circulation modeling, acquiring values peaking at about 700 J kg^{-1} , which implies vertical velocities of several tens of meters per second should the whole energy be released for the use of convection. We propose here to evaluate these parameters for the CO_2 meso-

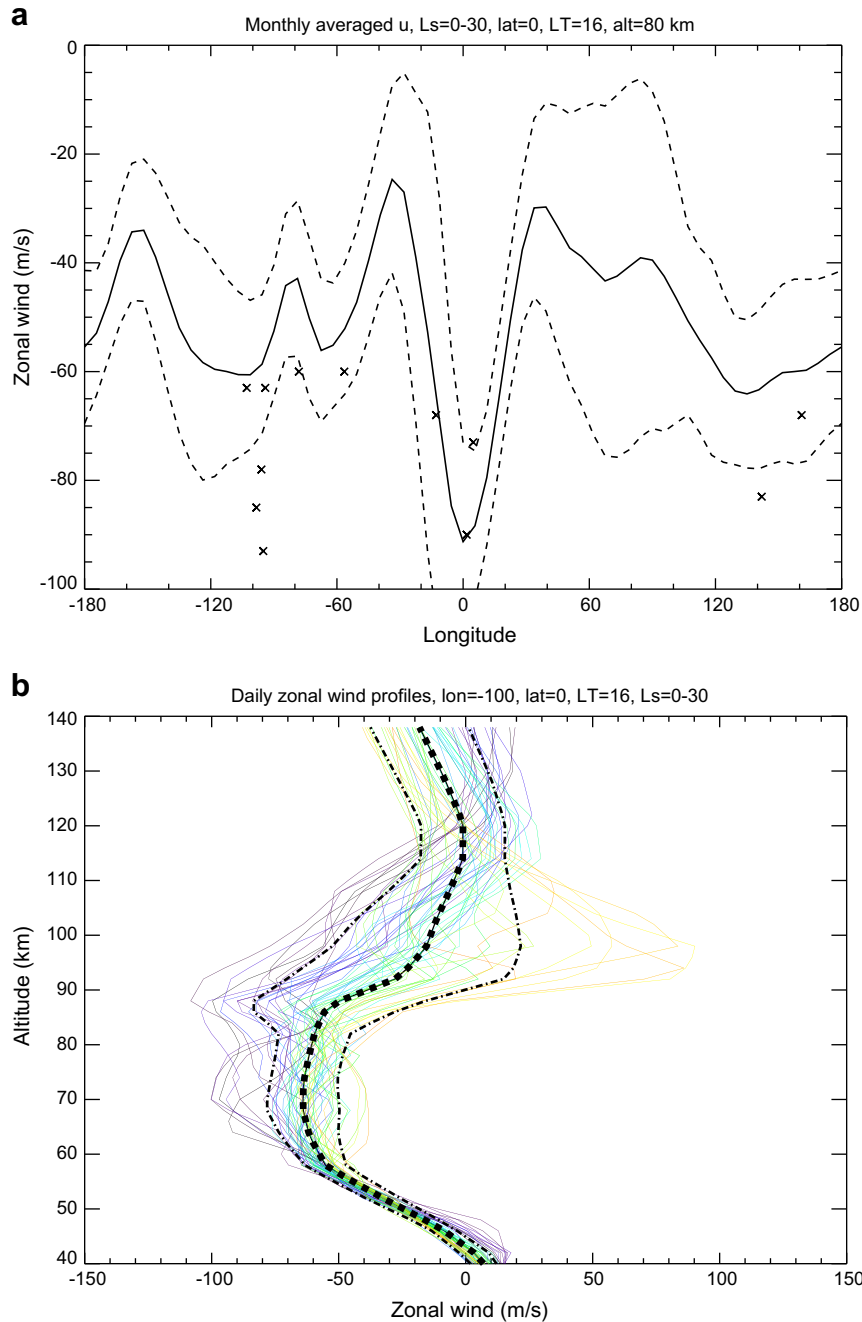


Fig. 13. (a) Monthly average of the zonal wind (solid line) at 80 km altitude at the equator for $L_s = 0-30^\circ$ and 16 local time. The dashed lines give the standard deviations and the crosses the HRSC observations. (b) The individual daily wind profiles at longitude 100°W at the equator for $L_s = 0-30^\circ$ and 16 local time. The solid line shows the monthly mean and dashed lines the standard deviation.

spheric clouds: in the light of the discussion of previous subsection, could large values of CAPE be reached at high altitudes?

Let us assume that in the CO_2 clouds the whole CAPE originates from the latent heat released when the atmospheric CO_2 condenses into ice particles. Should the radius r of the CO_2 particles be known, the cloud optical depth τ at wavelength λ_0 yields the total mass of condensates M in the atmospheric column according to the relationship $M = 4\tau\rho_{\text{ice}}r/3Q_{\text{ext}}$, where $\rho_{\text{ice}} \approx 1630 \text{ kg m}^{-3}$ is the density of CO_2 ice and Q_{ext} the extinction coefficient at wavelength λ_0 for particles of effective radius r . The CAPE then writes

$$\text{CAPE} = \frac{ML}{\rho_{\text{air}}A\Delta z} = \frac{4L}{3} \frac{r\tau}{Q_{\text{ext}}} \frac{1}{A\Delta z} \frac{\rho_{\text{ice}}}{\rho_{\text{air}}} \quad (3)$$

where $L \approx 5.9 \times 10^5 \text{ J kg}^{-1}$ is the CO_2 latent heat of condensation, ρ_{air} the atmospheric density in kg m^{-3} , A the surface of the convective cloud in m^2 and Δz its vertical extent in m.

In the two OMEGA orbits analysed in Section 3.4, typical values of $r \sim 1.5 \mu\text{m}$ and $\tau \sim 0.5$ (at $\lambda_0 = 1.4 \mu\text{m}$) are found in each pixel and correspond to the extinction factor $Q_{\text{ext}} \sim 3.5$ according to Mie theory computations. The area of each OMEGA pixel where CO_2 clouds are detected is $A = 3^2 \text{ km}^2$, the vertical extent of such clouds is estimated to 5–10 km and their altitude is $\sim 80 \text{ km}$, where $\rho_{\text{air}} \sim 10^{-6} \text{ kg m}^{-3}$. CAPE calculations show that a convective updraft cannot be as large as one OMEGA pixel, because the computed CAPE values are then negligible ($\sim 6 \times 10^{-3} \text{ J kg}^{-1}$), which contradict the existence of the convective updraft itself.

According to Eq. (3), what would be the extent and altitude of an hypothetical convective cell, given the radius and opacity estimated by OMEGA in this study? Fig. 14 (left panel) displays values of maximum vertical velocity w_{\max} calculated for various atmospheric density and convective cell sizes (corresponding CAPE estimates can be inferred from Eq. (2)). For the sake of illustration, the horizontal extent of the cell is assumed to be 10 times less than its vertical extent. The sedimentation vertical velocity w_{stokes} estimated from the Stokes–Rossow formula is superimposed in Fig. 14. In the area left of the dashed intersection line, the condensation of CO₂ yields convective updrafts which are likely to overwhelm the sedimentation processes, leading to the formation of a cumuliform CO₂ cloud. Fig. 14 (left panel) suggests that the convective columns that might form between 60 and 90 km and yield the observed CO₂ particles are more likely to be of ~10s to 100s meters size rather than 1000s meters size. The typical values of CAPE and vertical velocity that could be reached in such updrafts can be quite high, respectively 100s of J kg⁻¹ and 10s of m/s. Interestingly, Fig. 14 shows that the observed mesospheric clouds are very unlikely to be convective above 90 km (atmospheric density $\sim 2 \times 10^{-7}$ kg m⁻³), as the corresponding convective updrafts would concentrate the energy of the most severe storm on Earth (5000 J kg⁻¹) in a small volume of $200 \times 20 \times 20$ m³.

Discussions of Section 6.2 can be complemented by evaluating the supersaturation $\Delta T = T_{\text{parcel}} - T_{\text{env}} = T_{\text{sat}} - T$ associated to CAPE

values between 60 and 90 km. Eq. (2) is applied in a 3-km high CO₂ cloud at pressure 10^{-2} Pa (≈ 80 km), assuming constant ΔT over the cloud vertical extent. We found that values of ΔT no higher than 5 K would be necessary to yield values of CAPE of several hundreds of J kg⁻¹ (i.e. vertical velocity of several 10s m/s). Extreme updrafts (>100 m/s) and CAPE (>5000 J kg⁻¹) would be associated to supersaturation values of >30 K. Consider now values of supersaturation obtained in Section 6.2 for nucleation. Temperature deviations predicted for heterogeneous nucleation could yield significant values of CAPE and updraft velocity. Comparatively, extreme conditions required by homogeneous nucleation would induce very unlikely values of CAPE, associated to violent updrafts the plausibility thereof can be questioned.

For the sake of comparison, maximum vertical velocity calculations for CO₂ low-altitude clouds in polar regions ($r \sim 100$ μm, $\tau \sim 10$, $Q_{\text{ext}} \sim 2$) are shown in Fig. 14 (right panel). Compared to their high-altitude counterparts, the formation of those clouds seems to involve deeper and larger convective cores. For instance, in agreement with the numerical predictions by Colaprete et al. (2003), the vertical extent of 10 m s⁻¹ convective updrafts ~ 10 km above the surface ($\rho_{\text{air}} \sim 7 \times 10^{-3}$ kg m⁻³) is ~ 1 km in Fig. 14.

As a conclusion, if we assume the observed CO₂ cloud particles are of convective origin, the corresponding mesospheric clouds would be clusters of numerous small-scale intense convective

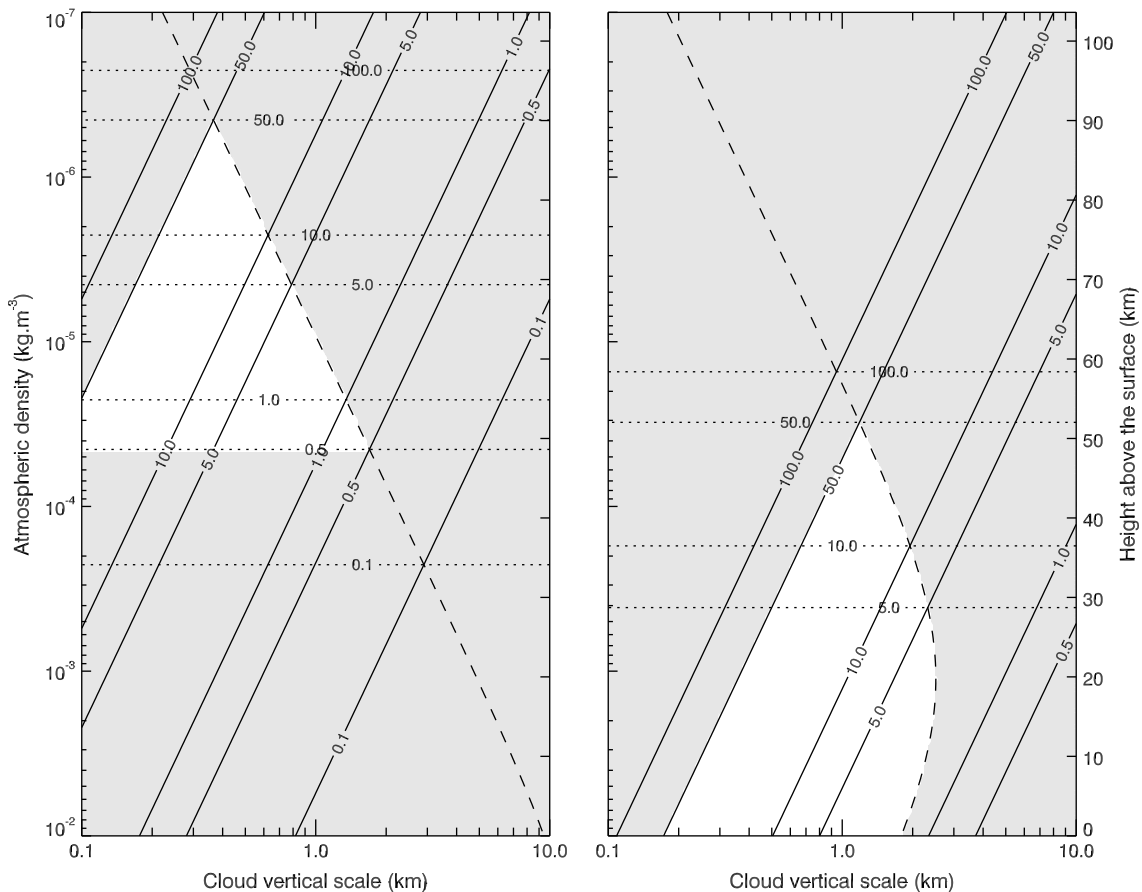


Fig. 14. Estimation of maximum convective vertical velocity $w_{\max} = \sqrt{2\text{CAPE}}$ as a function of the atmospheric density and the vertical extent of the convective cell. For the sake of illustration, the horizontal extent of the cell is assumed to be 10 times less than its vertical extent. The sedimentation vertical velocity w_{stokes} estimated from the Stokes–Rossow formula is superimposed as horizontal lines. The dashed line represents the “equilibrium” between the convective and sedimentation vertical velocities: left of this line, the convective motions overcome the sedimentation processes. White zones indicate the likely formation of convective structures in the simplified model we propose. Note that lower and upper limits of 0.5 m/s and 50 m/s for vertical velocity are considered to define convective updrafts, based on values encountered in terrestrial deep convection. On the left, typical properties for mesospheric CO₂ cloud particles are used in the computations: $r = 1.5$ μm, $\tau_{1.4\mu\text{m}} = 0.5$ and $Q_{\text{ext}}(1.4 \mu\text{m}) = 3.5$. On the right, typical properties for polar tropospheric CO₂ clouds are used: $r = 100$ μm, $\tau_{1.4\mu\text{m}} = 10$ and $Q_{\text{ext}}(1.4 \mu\text{m}) = 2$.

updrafts (even narrower than the kilometric extent of an OMEGA pixel) instead of a well-defined large and deep convective column. We suggest that the 5–10 km vertical extent of the cloud would likely result from various small-scale updrafts being triggered at various levels at the same time to form the deep convective appearance of the cloud. It could be possible that the CO₂ might be the martian counterpart of Mesoscale Convective Systems on Earth, the formation thereof is thought to involve “particle fountains” (Yuter and Houze, 1995). The formation of such localized cloudy convective clusters could be highly sensitive to the peculiar meteorological conditions of the considered regions, which might explain why the observation of martian cumuliform CO₂ clouds is particularly non-systematic.

It is obvious that the instructive dimensional analysis presented here does not allow us to be fully conclusive on the convective properties of the mesospheric CO₂ clouds. Such issues remain out of the scope of the present paper. “Cloud-resolving” simulations with a martian non-hydrostatic mesoscale model (e.g. Spiga and Forget, 2009) coupled with a CO₂ microphysical model are planned as future work to better understand the dynamics of the mesospheric CO₂ clouds and their possible convective nature.

7. Conclusions and summary

This paper reports three martian years of observations of mesospheric CO₂ clouds with the OMEGA and HRSC instruments on-board Mars Express. A 3σ detection method has been developed and the clouds have been mapped globally at all OMEGA orbits to acquire a comprehensive dataset of 60 cloud observations. The cloud occurrences in OMEGA data seem to show interannual variability, which is most probably related to a bias of the limited coverage of OMEGA observations. However, when looking at the whole 3-year dataset of OMEGA complemented by the observations of the HRSC, the equatorial clouds show a very similar behavior as the Clancy et al. (2007) MGS observations.

In our data, the equatorial clouds start appearing at or right after the northern spring equinox, but no observations have been made between $L_s = 60$ and 90° , except for one observation at $L_s = 87^\circ$. After the northern summer solstice the clouds reappear and form until $L_s = 120^\circ$, after which the activity clearly ceases and the clouds reappear only in very rare cases. Clancy et al. (2007) observed the reappearance of clouds after the aphelion season clearly later ($L_s = 110^\circ$) and they observed more clouds at the L_s range 120 – 170° . We have very recently observed what is most probably the first cloud of the new equatorial cloud season, at $L_s = 330^\circ$ in the end of MY 29.

The clouds are mainly observed between 150°W and 10°E with some cases around Tharsis Montes and Valles Marineris, but with most of the cases observed around Terra Meridiani on and at both sides of the prime meridian. Clancy et al. (2007) observed more clouds above Tharsis and they had a gap in longitude of observations between 30 and 50°W : our longitudinal distribution is more even between Terra Meridiani and Tharsis, but our observations are clearly focused around the prime meridian. The latitudinal distribution is quite constant with the clouds appearing mostly between 20°N and 20°S with three exceptions: orbit #567_0 at 50°S reported already by Montmessin et al. (2007) for OMEGA and here also seen by HRSC, orbit #0724_9 at 45°S observed by HRSC, and orbit #4358_6 at 45°N . These cases seem to belong to a winter midlatitude cloud class, reported for the northern hemisphere also by Inada et al. (2007) and McConnochie et al. (2009).

The mapping of the variations of the particle size within the clouds based on the observation of a two-peak structure in the spectral signature revealed that in 37% of the cases the second peak is absent, implying submicronic particle sizes. In 55% of the cases a

second peak was observed with higher intensity than the first peak, and thus in these cases the particle size exceeded $1\ \mu\text{m}$. In the remaining 8% of the cases a second peak was observed at 3σ , but it did not exceed the first peak in intensity. The interpretation of this result falls back to the submicronic particle size case. However, a comparison of two orbits with the effective radii analysed from the shadow observations revealed negligible correlation between the second-to-first peak ratio and the analysed radii: it seems that the spectral peak ratios cannot be used to directly analyse the particle sizes but a detailed fitting of the spectra is needed (out of the scope of this paper).

The two cases of cloud shadow observations at orbits #501_2 and #551_3 were thoroughly analysed using the method described already in Montmessin et al. (2007), but this time performing the analysis pixel-by-pixel. This allowed for mapping the cloud opacities and effective radii and their variations within the cloud. The maximum opacities reached were $\tau \approx 0.6$ with mean values of 0.14 and 0.25. The effective radii were found to lie mainly within 1 – $3\ \mu\text{m}$ with mean values of 2.1 and $2.3\ \mu\text{m}$. These results are in the same lines as the average results from the previous Montmessin et al. (2007) analysis, but we found that better fits were acquired with an effective variance $v = 0.2$.

The HRSC observations analysed showed cloud altitudes in the range 59 – $84\ \text{km}$ ($\pm 2\ \text{km}$), and in one case (SH midlatitude, orbit #0567_0) the cloud altitude was observed to change within the distance of several degrees latitude. The cloud altitude range is larger than that observed by MGS (Clancy et al., 2007), but the mean altitudes coincide well. The wind speeds observed were in general within the range of ~ 15 – $107\ \text{m/s}$ ($\pm 15\ \text{m/s}$) from east to west with only one measured case (#0567_0) of westerly winds in the southern midlatitudes showing varying wind speeds (5 – $42\ \text{m/s}$).

Previous comparisons with LMD-MGCM temperature fields (Montmessin et al., 2007) suggested that the model was not able to reach temperatures low enough as to allow for CO₂ condensation in the mesosphere. We performed a detailed inspection of the model results that showed a strong diurnal cycle of the temperatures at the altitudes of the observed clouds (65 – $85\ \text{km}$). This cycle was masked in the previous study (Fig. 12 in Montmessin et al. (2007)) by the diurnal average of the temperature field. However, the LMD-MGCM does not reach saturation at the observed cloud altitudes. In any case our study with the LMD-MGCM showed that, for $L_s = 0$ – 30 , the favoured time for CO₂ cloud formation between 65 and $85\ \text{km}$ of altitude is around the end of the afternoon because of the effect of thermal tides. In the early morning (4LT) the temperatures at these altitudes are at their warmest, inhibiting cloud formation (but allowing for cloud formation higher in the atmosphere). Most of the clouds have been observed in the afternoon, but the cases of early morning need to be looked at more in detail. In general the LMD-MGCM temperature minima match well the seasons and locations of the cloud observations (already mentioned by Clancy et al. (2007) and Montmessin et al. (2007)), even though supersaturations are not reached in the model. The LMD-MGCM winds and the HRSC observations of the cloud speeds are in good agreement, which is a very encouraging validation of the LMD-MGCM in an altitude range with very sparse observational data.

Cloud morphology was inspected with visual (by-eye) observation of the images, and in $\sim 15\%$ of the cases the clouds showed clearly clumpy, roundish, cumuliform shapes that were interpreted as convective type by Montmessin et al. (2007). In the rest of the cases the clouds either looked filamentary or the OMEGA image was too narrow for an accurate classification of the cloud. This analysis was complemented by simultaneous HRSC observations at some orbits. Most of the HRSC images show filamented, cirrus-type clouds with rare examples of complicated cloud morphologies with a roundish shape of the bulk cloud. An interesting feature is

that the round-shaped OMEGA clouds have been observed in the morning except for one early afternoon case (in the northern midlatitudes).

In the light of these sparse observations of round, clumpy clouds we have investigated the possibility of mesospheric convection on Mars with the help of convective potential calculations. Given the typical observed values for the effective radii and optical thicknesses, preliminary estimation of CAPE and convective vertical velocity suggests that the observed cumuliform clouds are more likely to be clusters of numerous small-scale intense convective updrafts than well-defined large and deep convective columns. Such small-scale convective cells might feature values of CAPE of 100s of J kg^{-1} and convective vertical velocity of 10s of m/s . These values can be attained with moderate temperature deviations from saturation at cloud formation, which can be induced by heterogeneous nucleation on small condensation nuclei.

Acknowledgments

We thank two anonymous reviewers for their comments that helped to improve the paper. A.M. gratefully acknowledges the post-doctoral funding from the Centre National d'Etudes Spatiales (CNES) and she also wishes to thank Dr. M. Douspis for sharing his insight in data analysis.

References

- Angelats i Coll, M., Forget, F., López-Valverde, M.A., Read, P.L., Lewis, S., 2004. Upper atmosphere of Mars up to 120 km: Mars Global Surveyor data analysis with the LMD general circulation model. *J. Geophys. Res.* 109, E01011. doi:10.1029/2003JE002163.
- Angelats i Coll, M., Forget, F., López-Valverde, M.A., González-Galindo, F., 2005. The first Mars thermospheric general circulation model: The martian atmosphere from the ground to 240 km. *Geophys. Res. Lett.* 32, L04201. doi:10.1029/2004GL021368.
- Bibring, J.-P., 42 colleagues, and the OMEGA Co-I Team, 2004. OMEGA: Observatoire pour la minéralogie, l'eau, les glaces et l'activité. ESA SP-1240: Mars Express: The Scientific Payload, pp. 37–49.
- Bougher, S.W., Engel, S., Roble, R.G., Foster, B., 1999. Comparative terrestrial planet thermosphere. 2. Solar cycle variation of global structure and winds at equinox. *J. Geophys. Res.* 104 (E7), 16591–16611.
- Clancy, R.T., Wolff, M.J., Whitney, B.A., Cantor, B.A., Smith, M.D., 2007. Mars equatorial mesospheric clouds: Global occurrence and physical properties from Mars Global Surveyor Thermal Emission Spectrometer and Mars Orbiter Camera limb observations. *J. Geophys. Res.* 112, E04004. doi:10.1029/2006JE002805.
- Colaprete, A., Toon, O.B., 2002. Carbon dioxide snow storms during the polar night on Mars. *J. Geophys. Res.* 107 (E7).
- Colaprete, A., Toon, O.B., 2003. Carbon dioxide clouds in an early dense martian atmosphere. *J. Geophys. Res.* 108 (E4).
- Colaprete, A., Haberle, R.M., Toon, O.B., 2003. Formation of convective carbon dioxide clouds near the south pole of Mars. *J. Geophys. Res.* 108 (E7).
- Colaprete, A., Barnes, J.R., Haberle, R.M., Montmessin, F., 2008. CO₂ clouds, CAPE and convection on Mars: Observations and general circulation modeling. *Planet. Space Sci.* 56, 150–180. doi:10.1016/j.pss.2007.08.010.
- Evans, K.F., 1998. The spherical harmonics discrete ordinate method for three-dimensional atmospheric radiative transfer. *J. Atmos. Sci.* 55, 429–446.
- Forget, F., Hourdin, F., Fournier, R., Hourdin, C., Talagrand, O., Collins, M., Lewis, S.R., Read, P.L., Huot, J.-P., 1999. Improved general circulation models of the martian atmosphere from the surface to above 80 km. *J. Geophys. Res.* 104, 24155–24176.
- Forget, F., Montmessin, F., Bertaux, J.-L., González-Galindo, F., Lebonnois, S., Quémerais, E., Reberac, A., Dimarellis, E., López-Valverde, M.A., 2009. The density and temperatures of the upper martian atmosphere measured by stellar occultations with Mars Express SPICAM. *J. Geophys. Res.* 114, E01004. doi:10.1029/2008JE003086.
- Formisano, V., Maturilli, A., Giuranna, M., D'Aversa, E., López-Valverde, M.A., 2006. Observations of non-LTE emission at 4–5 microns with the Planetary Fourier Spectrometer aboard the Mars Express mission. *Icarus* 182, 51–67.
- González-Galindo, F., Forget, F., López-Valverde, M.A., i Coll, M.A., Millour, E., 2009. A ground-to-exosphere martian general circulation model: 1. Seasonal, diurnal and solar cycle variation of thermospheric temperatures. *J. Geophys. Res.* 114, E04001. doi:10.1029/2008JE003246.
- Holton, J.R., 1992. *An Introduction in Dynamic Meteorology*. Academic Press, San Diego, CA.
- Inada, A., Richardson, M.I., McConnochie, T.H., Strausberg, M.J., Wang, H., Bell III, J.F., 2007. High-resolution atmospheric observations by the Mars Odyssey Thermal Emission Imaging System. *Icarus* 192, 378–395.
- Ivanov, A.B., Muhleman, D.O., 2001. Cloud reflection observations: Results from the Mars Orbiter Laser Altimeter. *Icarus* 154, 190–206.
- Jaumann, R., and 24 colleagues, 2007. The High Resolution Stereo Camera (HRSC) experiment on Mars Express: Instrument aspects and experiment conduct from interplanetary cruise through the nominal mission. *Planet. Space Sci.* 55, 928–952. doi:10.1016/j.pss.2006.12.003.
- Jouglet, D., Poulet, F., Langevin, Y., Bibring, J.-P., Gondet, B., Vincendon, M., Berthe, M., 2008. OMEGA long wavelength channel: Data reduction during non-nominal stages. *Planet. Space Sci.* 57, 1032–1042. doi:10.1016/j.pss.2008.07.025.
- Lee, C., and 12 colleagues, 2009. Thermal tides in the martian middle atmosphere as seen by the Mars Climate Sounder. *J. Geophys. Res.* 114, E03005. doi:10.1029/2008JE003285.
- Lefèvre, F., Lebonnois, S., Montmessin, F., Forget, F., 2004. Three-dimensional modeling of ozone on Mars. *J. Geophys. Res.* 109, E07004. doi:10.1029/2004JE002268.
- Määttänen, A., Vehkamäki, H., Lauri, A., Merikallio, S., Kauhainen, J., Savijärvi, H., Kulmala, M., 2005. Nucleation studies in the martian atmosphere. *J. Geophys. Res.* 110, E02002.
- McConnochie III, T.H., Bell, J.F., Savransky, D., Wolff, M.J., Toigo, A.D., Wang, H., Richardson, M.I., Christensen, P.R., 2009. THEMIS-VIS observations of clouds in the martian mesosphere: Altitudes, wind speeds, and decameter-scale morphology. *Icarus*, submitted for publication.
- Montmessin, F., Forget, F., Rannou, P., Cabane, M., Haberle, R.M., 2004. Origin and role of water ice clouds in the martian water cycle as inferred from a general circulation model. *J. Geophys. Res.* 109, E10004.
- Montmessin, F., and 10 colleagues, 2006a. Subvisible CO₂ clouds detected in the mesosphere of Mars. *Icarus* 183, 403–410.
- Montmessin, F., Quémerais, E., Bertaux, J.-L., Korabiev, O., Rannou, P., Lebonnois, S., 2006b. Stellar occultations at UV wavelengths by the SPICAM instrument: Retrieval and analysis of martian haze profiles. *J. Geophys. Res.* 111, E09S09. doi:10.1029/2005JE002662.
- Montmessin, F., Gondet, B., Bibring, J.-P., Langevin, Y., Drossart, P., Forget, F., Fouchet, T., 2007. Hyper-spectral imaging of convective CO₂ ice clouds in the equatorial mesosphere of Mars. *J. Geophys. Res.* 112. doi:10.1029/2007JE002944.
- Noel, V., Hertzog, A., Chepfer, H., 2009. CALIPSO observations of wave-induced PSCs with near-unity optical depth over Antarctica in 2006–2007. *J. Geophys. Res.* 114, D05205. doi:10.1029/2008JD010604.
- Pettengill, G.H., Ford, P.G., 2000. Winter clouds over the north martian polar cap. *Geophys. Res. Lett.* 27 (5), 609–612.
- Pruppacher, H.R., Klett, J.D., 1997. *Microphysics of Clouds and Precipitation*. Kluwer Academic Publishers, Dordrecht.
- Scholten, F., Hoffmann, H., Määttänen, A., Montmessin, F., Gondet, B., Hauber, E., 2010. Concatenation of HRSC colour and OMEGA data for the determination and 3D-parameterization of high-altitude CO₂ clouds in the martian atmosphere. *Planet. Space Sci.*, in press. doi:10.1016/j.pss.2010.04.015.
- Smith, M., Wolff, M., Spanovich, N., Ghosh, A., Banfield, D., Christensen, P., Landis, G., Squyres, S.W., 2006. One martian year of atmospheric observations using MER mini-TES. *J. Geophys. Res.* 111, E12S13. doi:10.1029/2006JE002770.
- Spiga, A., Forget, F., 2009. A new model to simulate the martian mesoscale and microscale atmospheric circulation: Validation and first results. *J. Geophys. Res.* 114, E02009.
- Vehkamäki, H., 2006. *Classical Nucleation Theory in Multicomponent Systems*. Springer, Berlin/Heidelberg.
- Vehkamäki, H., Määttänen, A., Lauri, A., Napari, I., Kulmala, M., 2007. Technical note: The heterogeneous zeldovich factor. *Atmos. Chem. Phys.* 7, 309–313.
- Wood, S.E., 1999. *Nucleation and Growth of CO₂ Ice Crystals in the Martian Atmosphere*. Ph.D. Thesis, University of California, Los Angeles.
- Yuter, S.E., Houze, R.A., 1995. Three-dimensional kinematic and microphysical evolution of florida cumulonimbus. Part III: Vertical mass transport, maw divergence, and synthesis. *Mon. Weather Rev.* 123, 1964–1983.